



KOCAELI JOURNAL OF SCIENCE AND ENGINEERING

(2018)

Çk bYf

Prof. Dr. Sadettin HÜLAGÜ - (Kocaeli University)

Editor in Chief

Prof. Dr. K. Süleyman YİĞİT - (Kocaeli University)

Associate Editors

Prof. Dr. Murat HOŞÖZ - (Kocaeli University)

Assoc. Prof. Dr. H. Hakan GÜREL - (Kocaeli University)

Production Editor

Instructor Yusuf YAĞCI - (Kocaeli University)

Assistant Editors

R. A. Abdurrahman GÜN - (Kocaeli University)

R. A. Alp Eren ŞAHİN - (Kocaeli University)

Copy Editor (English)

Şahin Alp Eren ŞAHİN - (Kocaeli University)

GWYUf m

Özlem ŞAHİN - (Kocaeli University)

Section Editors

ALADAĞ Zerrin, (Prof. Dr.) - (Kocaeli University, TR)
ARİK Mehmet, (Prof. Dr.) - (Özyeğin University, TR)
ATUN Ata, (Prof. Dr.) - (Cyprus Science University, KKTC)
AZEVEDO Helena, (Dr.) - (Queen Mary University of London, ENG)
CASTILLO Oscar, (Prof. Dr.) - (Tijuana Institute of Technology, MEX)
CIVAN Mihriban, (Asst. Prof. Dr.) - (Kocaeli University, TR)
ÇANAĞCI Mustafa, (Prof. Dr.) - (Kocaeli University, TR)
DUNFORD Nurhan Turgut, (Prof. Dr.) - (Oklahoma State University, USA)
ENGİN Tahsin, (Prof. Dr.) - (Sakarya University, TR)
ERDEMLİ Yunus Emre, (Prof. Dr.) - (Kocaeli University, TR)
ERTUNÇ H. Metin, (Prof. Dr.) - (Kocaeli University, TR)
FIĞLALI Nilgün, (Prof. Dr.) - (Kocaeli University, TR)
GÖKTAŞ Recep Kaya, (Prof. Dr.) - (Kocaeli University, TR)
GÜLTEKİN Fatma, (Prof. Dr.) - (Karadeniz Technical University, TR)
GÜRAY Ünal Taygun, (Prof. Dr.) - (Kocaeli University, TR)
KASIM Tamer, (Assoc. Prof. Dr.) - (Kocaeli University, TR)
KİSHALİ Emre, (Asst. Prof. Dr.) - (Kocaeli University, TR)
ORUÇ Bülent, (Prof. Dr.) - (Kocaeli University, TR)
ÖZDEMİR Engin, (Prof. Dr.) - (Kocaeli University, TR)
ÖZTÜRK Günay, (Assoc. Prof. Dr.) - (Kocaeli University, TR)
PEKEY Beyhan, (Prof. Dr.) - (Kocaeli University, TR)
SAYAR Ahmet, (Assoc. Prof. Dr.) - (Kocaeli University, TR)
SINMAZÇELİK Tamer, (Prof. Dr.) - (Kocaeli University, TR)
SOPIAN Kamaruzzaman, (Prof. Dr.) - (The National University of Malaysia, MAL)
SOSTAKS Aleksandrs, (Prof. Dr.) - (University of Latvia, LV)
SÖZEN Adnan, (Prof. Dr.) - (Gazi University, TR)
STANASEL Iulian, (Assoc. Prof. Dr.) - (University of Oradea, RO)
ŞAHİN Ahmet Zâde, (Prof. Dr.) - (KFUPM, SA)
ŞAHİN Suhap, (Prof. Dr.) - (Kocaeli University, TR)

Advisory Board

AKIN Nilgün, (Prof. Dr.) - (Kocaeli University, TR)
ARI Ayşe Arzu, (Asst. Prof. Dr.) - (Kocaeli University, TR)
ARICI Müslüm, (Assoc. Prof. Dr.) - (Kocaeli University, TR)
ATAPEK Hakan, (Assoc. Prof. Dr.) - (Kocaeli University, TR)
BAYNAL Kasım, (Assoc. Prof. Dr.) - (Kocaeli University, TR)
ÇEPNİ Murat Selim, (Assoc. Prof. Dr.) - (Kocaeli University, TR)
ÇETKİN Vildan, (Asst. Prof. Dr.) - (Kocaeli University, TR)
ÇOBAN Onur, (Asst. Prof. Dr.) - (Kocaeli University, TR)
COŞKUN Safa Bozkurt, (Prof. Dr.) - (Kocaeli University, TR)
DEMİR Arif, (Prof. Dr.) - (Kocaeli University, TR)
ENGİN Şeref Naci, (Prof. Dr.) - (Yıldız Technical University, TR)
EREN Canan Dilek, (Asst. Prof. Dr.) - (Kocaeli University, TR)
ERGÜL Halim AYTEKİN, (Assoc. Prof. Dr.) - (Kocaeli University, TR)
GENÇ Nevim, (Prof. Dr.) - (Kocaeli University, TR)
GÜNDOĞDU Özcan, (Prof. Dr.) - (Kocaeli University, TR)
İPLİKÇİ Serdar, (Prof. Dr.) - (Pamukkale University, TR)
KANDEMİR İlyas, (Assoc. Prof. Dr.) - (Gebze Technical University, TR)
KARAKAŞ Ahmet, (Assoc. Prof. Dr.) - (Kocaeli University, TR)
KASIM Rezzan, (Prof. Dr.) - (Kocaeli University, TR)
KILIÇARSLAN Ali, (Prof. Dr.) - (Hitit University, TR)
KÖKER Raşit, (Prof. Dr.) - (Sakarya University, TR)
KUYUMCU Feriha Erfan, (Prof. Dr.) - (Kocaeli University, TR)
KÜRÜM Hasan, (Prof. Dr.) - (Firat University, TR)
ONAT Burcu, (Assoc. Prof. Dr.) - (Istanbul University, TR)
ÖZER Nil Pembe, (Prof. Dr.) - (Kocaeli University, TR)
SAYIN Cenk, (Prof. Dr.) - (Marmara University, TR)
SERTÇELİK Fadime, (Prof. Dr.) - (Kocaeli University, TR)
SÜRMEİLİ Hikmet, (Assoc. Prof. Dr.) - (Mersin University, TR)
SÜRMEİN Ali, (Prof. Dr.) - (Uludağ University, TR)
TOKAT Sezai, (Prof. Dr.) - (Pamukkale University, TR)
URHAN Oğuzhan, (Prof. Dr.) - (Kocaeli University, TR)
YILMAZ Mehmet, (Prof. Dr.) - (Kocaeli University, TR)
YİĞİT Halil, (Assoc. Prof. Dr.) - (Kocaeli University, TR)

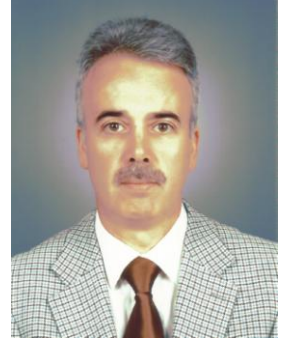
Printed By

Kocaeli University - Graduate School of Natural and Applied Sciences - Umuttepe Campus 41380, Kocaeli / TURKEY

Tel: +090 (262) 303 35 56 Fax: +090 (262) 303 30 33 E-mail: kojose@kocaeli.edu.tr

EDITORIAL

It is our proud to inform all our readers that, starting from 2019 issues, Kocaeli Journal of Science and Engineering (KOJOSE) has been accepted to be indexed by TR Dizin. Considering that KOJOSE have been publishing issues for only three years, it is a great opportunity and success for us to be indexed by TR Dizin, the unique index of Turkey. In the next terms, we will do our best to be indexed by the prestigious international indexes.



In this regard, I would like to express my deep gratitude and appreciation to the Rector of Kocaeli University, Prof. Dr. Sadettin Hülügü, for his continuous support and encouragement. I also would like to thank Associate Editors Prof. Dr. Murat Hoşöz and Assoc. Prof. Dr. Hikmet Hakan Gürel for their invaluable efforts in various stages of preparing the journal. Our Production Editor Expert Yusuf Yağcı, Assistant Editors R. A. Abdurrahman Gün and R. A. Alp Eren Şahin, Copy Editor Lecturer İsmail Hakkı Paslı, Secretary Durmuş İmat, all Section Editors, Advisory Board Members as well as our Authors and Reviewers also have share in our success, and they deserve deep appreciation.

As a result of the significant disruption caused by the COVID19 pandemic, many journals including KOJOSE have difficulty in meeting the publishing timelines. Therefore, we publish our first 2020 issue with a little delay. The new issue of the KOJOSE contains four papers from the disciplines of automotive engineering, mechanical engineering, mechatronics engineering and energy engineering. I would like to thank to all our authors and reviewers of this issue.

Finally, I would like to invite the investigators and scientists from the related branches of science and engineering to submit their best studies for publication in KOJOSE.

Prof. Dr. Kadri Süleyman Yiğit
Editor in Chief



COVER PAGE	I
EDITORIAL AND ADVISORY BOARDS.....	II
EDITORIAL	III
TABLE OF CONTENTS	IV

Ali AMİNİ, Baybars ÖZELCİ, Tanlay ÖZDEMİR, Özgür EKİCİ, S. Çağlar BAŞLAMIŞLI, Murat KÖKSAL

Experimental Study of the Performance of a Li-ion Battery Cell in a Highway Driving Cycle..... 01-08

(Research Paper)

Zehranur YILMAZ, Orkun YILMAZ, Zafer BİNGÜL

Design, Analysis and Simulation of a 6-DOF Serial Manipulator 09-15

(Research Paper)

Ebubekir BEYAZOĞLU, Erhan PULAT

Turbulence Modelling on Fluidized Bed Gasification..... 16-26

(Research Paper)

Kasım TOPRAK, Ahmet Berk YILMAZ

Non-equilibrium Molecular Dynamics for Calculating the Thermal Conductivity of Graphene-Coated Aluminum..... 27-32

(Research Paper)



Experimental Study of the Performance of a Li-Ion Battery Cell in a Highway Driving Cycle

Ali AMİNİ^{1,*} , Baybars ÖZELCİ² , Tanlay ÖZDEMİR³ , Özgür EKİCİ⁴ , S. Çağlar BAŞLAMIŞLI⁵ ,
Murat KÖKSAL⁶ 

¹Department of Mechanical Engineering, Hacettepe University, Ankara, 06800, Turkey, **ORCID:** 0000-0002-4668-5258

²Department of Mechanical Engineering, Hacettepe University, Ankara, 06800, Turkey, **ORCID:** 0000-0003-2649-8612

³Department of Mechanical Engineering, Hacettepe University, Ankara, 06800, Turkey, **ORCID:** 0000-0003-1692-9781

⁴Department of Mechanical Engineering, Hacettepe University, Ankara, 06800, Turkey, **ORCID:** 0000-0002-1370-7190

⁵Department of Mechanical Engineering, Hacettepe University, Ankara, 06800, Turkey, **ORCID:** 0000-0002-7476-2257

⁶Department of Mechanical Engineering, Hacettepe University, Ankara, 06800, Turkey, **ORCID:** 0000-0003-1509-2246

Article Info

Research paper

Received : December 31, 2019

Accepted : June 30, 2020

Keywords

Driving Cycle
Electric Vehicle
Li-Ion Battery
Thermal Behavior

Abstract

Li-ion batteries, as a secondary battery type, are currently the most viable option for powering hybrid/electric vehicles. They have considerable advantages such as high specific energy and power, no memory effect, long cycling life, low maintenance requirement, and low self-discharge rate. However, their thermal performance can easily deteriorate at extreme ambient temperatures. Therefore, in this study, thermal and electrical behaviors of Li-ion batteries were investigated under various operating temperatures using a driving cycle that represents a highway driving condition. A battery testing system was used to determine the performance of Li-ion batteries under simulated loads. The results show that the measured temperature profiles, in broad strokes, follow the current profile. Because of the thermal capacitance of the battery, the changes in temperature variations are observed to be the smoothed out version of the current profile. Moreover, the results show that the extreme ambient temperatures have adverse effects on thermal performance of Li-ion batteries. The volumetric energy density and the capacity of the cell significantly decrease at cold ambient temperatures, especially for the sub-zero temperature applications possibly due to weak ionic conductivity within the cell. On the other hand, the difference between the ambient temperature and the surface of the cell becomes more pronounced as the ambient temperature decreases.

1. Introduction

Li-ion batteries have been widely using in electric vehicles and most of the portable electronic devices since they offer higher energy density, higher cycling life, and low self-discharge rate compared to the other power sources [1]. There are various studies related to improving the energy density and capacity of the Li-ion batteries in order to increase the acceleration rate and the driving range of the electric vehicles. However, as the energy requirement from the Li-ion batteries continues to develop, the safety risk increases as well.

Safety concerns on Li-ion batteries are mostly related to the thermal behavior of the battery. Pesaran et al. stated that the operating temperature range of Li-ion batteries should be kept between 15-35 °C since both high and low temperatures have adverse effects on Li-ion batteries thermal performance [2]. The increment of operating temperature can produce severe degradation problems and reduce battery lifespan [2]. Using of battery cells in pack design requires more attention to temperature distribution. Thermal management in this kind of design is utilized by cooling systems. Poor conductivity of cell stack to the cooling plate and asymmetric design of battery cells can affect on the performance of battery cells significantly [3].

Motloch et al. indicated that within the temperature range of 30-40°C, each increment of working temperature

* Corresponding Author: ali82amini@gmail.com

This article is an extended version of the paper presented at the 22nd Congress on Thermal Science and Technology.



caused a reduction in battery life approximately two months [4].

Elevated operating temperatures can cause a capacity fade of the Li-ion cell as the cell is cycled. Ramadass et al. cycled a Sony 18650 Li-ion cell both at room temperature and at 45°C and found the capacity of the cell at 45°C decreased 6% more after 800 cycles [5]. As an extreme condition, if the temperature within the cell reaches a point in which the exothermic side reactions can be triggered, these reactions exponentially increase the heat generation within the cell and may lead to a possible thermal runaway condition [6].

Li-ion batteries are preferred due to their high volumetric energy density values, which provide the user to manage the working area effectively. However, the volumetric energy density of the cell significantly decreases at cold ambient temperatures, particularly for the subzero temperature applications. Nagasubramanian examined the energy density of a 18650 Panasonic Li-ion cell in a temperature range between -40°C and 25°C. He found that the volumetric energy density of the cell was reduced to 95% at -40°C compared to that at room temperature [7].

Jaguemont et al. performed an experiment at 50 A discharging current and demonstrated that the energy that could be obtained from a 100-Ah LiFeMnPO₄ Li-ion cell reduced from 302 Wh to 183 Wh as the ambient temperature decreased from the room temperature to the -25°C [8]. Huo et al. investigated the thermal behavior of a Li-ion cell at various ambient temperatures during a galvanostatic discharging process and observed that the temperature gradient at the surface center of the cell became sharper as the temperature decreased [1].

There are few studies that investigated the battery thermal behavior under driving cycle loads. Tourani et al. composed a combination of ECE15 and EUDC driving cycles to test their battery model that was working under normal ambient conditions [9]. They estimated the temperature variation of battery cell and verified that by experimental data. Panchal et al. investigated electrical and thermal behavior of lithium-ion battery package of vehicle travelling on both highway and city driving cycle [10]. The ambient temperature was between 2-17°C in this comprehensive study [10].

To the best of authors' knowledge, there is no study that addresses the thermal behavior of battery cell under driving cycle load working in different ambient conditions.

In this experimental study, first, a battery testing system was used to determine the surface temperature of the cell at given current inputs during charging or discharging processes of the driving cycle. Then, FTP-Highway (Federal Test Procedure) driving cycle was simulated by applying the corresponding current values to

the Li-ion cell in order to investigate the thermal behavior of the battery under various operating conditions.

2. Materials and Methods

2.1. Experimental Setup and Procedure

An experimental setup was established in order to investigate the thermal behavior of the Panasonic NCR18650B cylindrical Li-ion battery cells under driving cycle loads, which is shown in Figure 1. A battery test stand was designed in a way to test 4 battery cells simultaneously. Figure 1(a) shows the battery-testing device (Maccor 4300) which was used to determine the quality and performance of Li-ion batteries by applying simulated loads under computer control. The surface temperature of the cell was measured by T-type thermocouples as shown in Figure 1(b). According to previous studies, the maximum temperature difference between surface and center of battery cells during charge/discharge process are not significant. Also, a single temperature measurement point can provide adequate data regarding battery thermal behavior [11].

The thermocouples were connected to the NI (National Instrument) USB 6341 data acquisition device. Special design of clamp was used to minimize the contact resistance between battery surface and thermocouple tip.

First of all, a set of galvanostatic tests were done in different charge and discharge current values. Testing time was lasted 30, 60 and 90 minutes, depending on C rate values. The C-rate is a measure of the rate at which a battery is being charged or discharged.

In the second step, a specific current profile was generated by the vehicle model and was loaded to the battery-testing device. Every driving cycle test for a single battery was composed of 5 cycles and lasted 64 minutes.

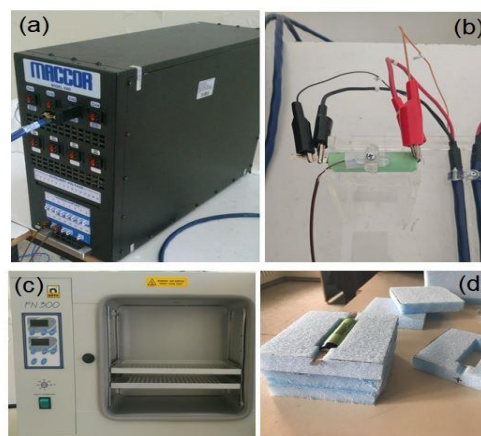


Figure 1. Experimental set-up (a) battery test device (b) battery cell test stand (c) oven (d) insulation around a battery.

Experiments were done for various operating temperatures: -20, 0, 20, 40, and 60 °C. A refrigerator and a natural convection oven as shown in Figure 1(c) were used to provide the required ambient temperatures during the experiments. Moreover, a nearly adiabatic operating condition was simulated using a foam insulation around the cell as shown in Figure 1(d). All tests were carried out simultaneously for 4 different battery cells to detect and prevent possible installation and measurement errors.

2.2. Modelling

2.2.1. Vehicle Dynamic Model

An electric vehicle model was constructed in MATLAB/Simulink environment. In this model, power request of vehicle was calculated according to tractive force, inertial, rolling and air resistance forces. Detailed explanation about the resistance forces calculation can be found in Boyalı et al. [12]. Efficiency map of electric motor was

assumed as a function of its torque and angular speed. Battery modeling was also implemented using an equivalent circuit diagram, where battery internal resistance is a function of state of charge (SoC). The electrical current drawn from the battery during charging and discharging situations was calculated with the following equations [12];

$$I_{\text{chg}} = \frac{-V_{\text{ocv}} + \sqrt{V_{\text{ocv}}^2 + 4R_i P_{\text{chg}}(t)}}{2R_i} \quad (1)$$

$$I_{\text{dis}} = \frac{V_{\text{ocv}} - \sqrt{V_{\text{ocv}}^2 - 4R_i P_{\text{dis}}(t)}}{2R_i} \quad (2)$$

In Eq. (1) and Eq. (2), $P_{\text{chg}}(t)$, $P_{\text{dis}}(t)$ are the charge loads during charging and discharging at the battery terminal, V_{ocv} , open circuit voltage and R_i are internal resistances of the battery.

Vehicle dynamic model is summarized in Figure 2 and Figure 3.

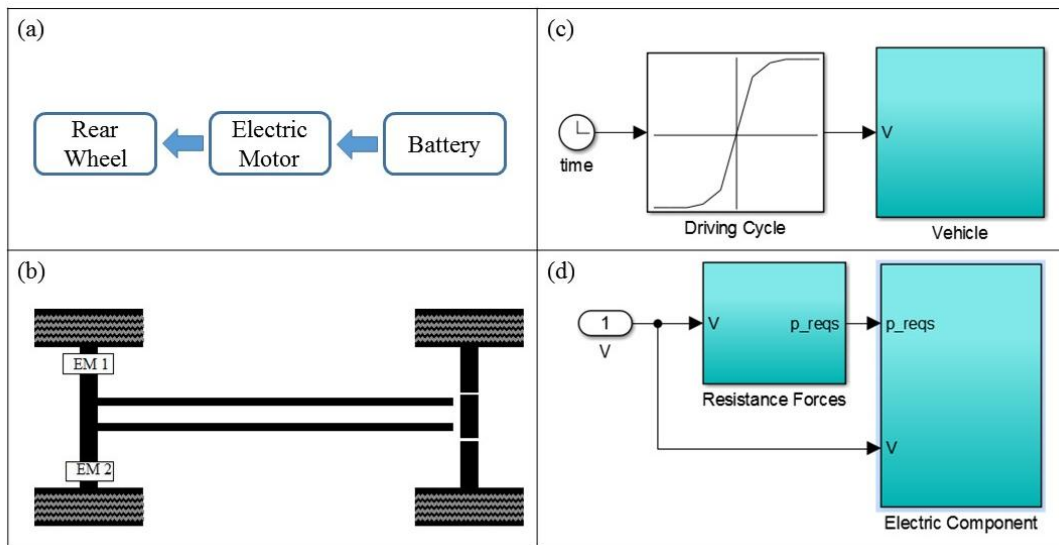


Figure 2. Vehicle architecture (a) energy flow (b) vehicle structure (c) reverse vehicle model (d) vehicle dynamic blocks.

Figure 2(a) illustrates the energy flow in vehicle model. The position of electric motors and their connection with rear wheels are shown in Figure 2(b). Figure 2(c) and Figure 2(d) show the reverse vehicle model. Over the time steps, driving cycle box sends velocity values to the vehicle model and the desired torque and speed values are calculated for electric motor to proceed to the next step (Figure 3). According to resistance force values, it is possible to calculate the time variant velocity and requested torque of vehicle. By knowing the speed reduction ratio, the speed and torque values of electric

motor are calculated. By considering the efficiency of electric motor, it is possible to calculate the battery electric power. In battery sub model, equivalent circuit diagram was composed to find the battery voltage and current values.

2.2.2. Vehicle Parameters

The specifications of a prototype electric vehicle model are given in Table 1. The parameters were selected according to the Hybrid/Electric prototype vehicle that was

designed in Hacettepe University Senstech Laboratory. It consists of two hub electric motors in front wheels. Also, the battery package was selected according to current and voltage limits of Maccor testing system.

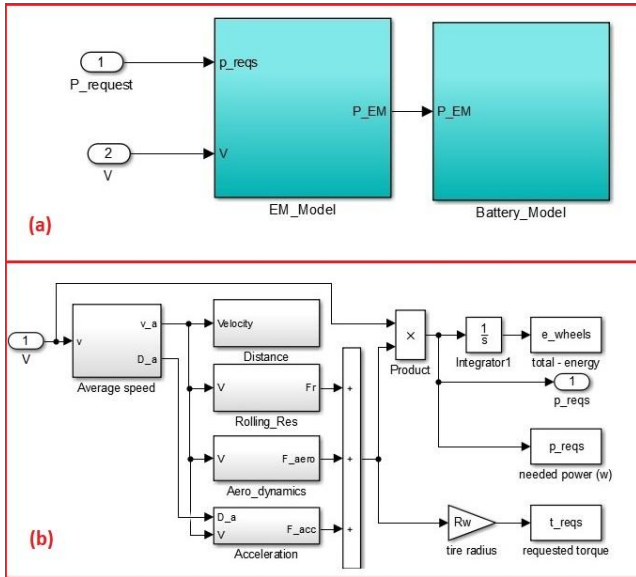


Figure 3. Detailed view of vehicle model (a) electric motor and battery (b) resistance forces.

Table 1. Prototype electric vehicle parameters.

Element	Parameter	Value
Vehicle	Mass	400 [kg]
	Air Resistance Coefficient	0.5
	Air Density	1.24 [kg/m ³]
	Frontal Area	2 [m ²]
	Wheel Radius	0.2925 [m]
Gearbox	Gear Ratio	1
	Final Drive Ratio	1
	Transmission Efficiency	0.99
Electric Motor	Maximum Torque	2 x 270 [Nm]
	Maximum Power	2 x 13.7 [kW]
	Maximum Angular Velocity	570 [RPM]
Battery Package (24s x 35p)	Capacity	114 [Ah]
	Open Circuit Voltage	100 [V]
	Maximum Current	175 [A]
Battery Cell	Capacity	3.25 [Ah]
	Open Circuit Voltage	4.2 [V]
	Maximum Current	5 [A]

2.2.3. Driving Cycle

In order to examine the battery cell reaction for different operating conditions, ‘FTP-Highway’ driving cycle was used in EPA [13]. Vehicle speed and traveled distance in this condition are shown in Figure 4. According to simulation results, battery cell parameters variation is

shown in Figure 5. The current profile of the battery cell was used as input data in experimental studies.

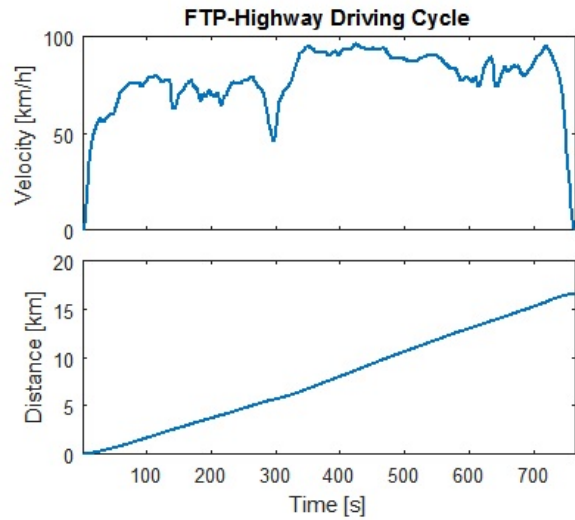


Figure 4. Variation of the velocity and distance with time in the driving cycle.

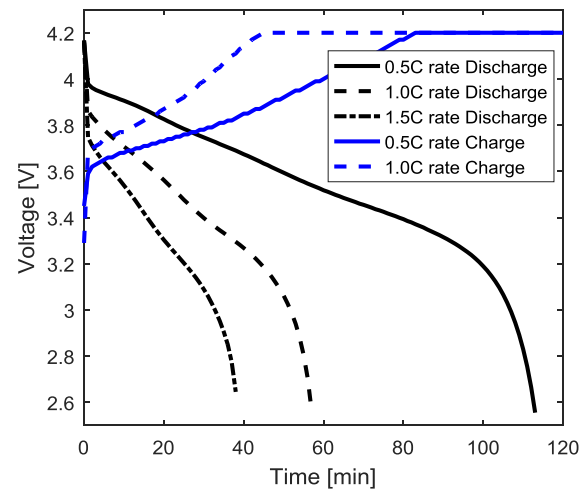


Figure 5. Voltage variation for different galvanostatic discharge/charge applications.

3. Results and Discussion

3.1. Galvanostatic Charge/Discharge

Before starting the planned tests within the scope of the study, various test measurements were performed in order to test the accuracy of measurement equipment. In the first step, voltage-time values for 18650 Li-Ion batteries in different galvanostatic (constant current) discharge/charge modes were measured and presented in Figure 6. Discharge tests were done at typical values of 0.5C, 1.0C, and 1.5C rates. As it is known, the 1.0C discharge rate refers to the constant current for discharging a full capacity of a battery in one hour. For Panasonic NCR18650B battery cell, this constant current value is

3.25 A. Since the maximum current value allowed by the Maccor testing system in our laboratory is 5.0 A, the upper current value for the discharge tests was limited to 1.5C rate. The termination of discharge test was performed automatically when the minimum voltage was reached to 2.5 V, which is the permitted voltage that is recommended by the battery manufacturer. Charge tests were done at typical values of 0.5C, 1.0C rates (0.5C rate is the ideal current that is recommended by the battery manufacturer). As it can be seen in Figure 5, the termination of the charge process was determined by a voltage limit similar to discharge process. As seen in Figure 5, except the beginning and ending time of charge/discharge processes, battery cell voltage has a linear dependency with time. One of the main differences that can be observed in charge and discharge applications is the progression of the process approaching the end time. Voltage is limited to 4.2 V towards the end of the charging process. However, in discharging, voltage variation is sharper at the end of the process. As a result, the values presented in Figure 5 show the expected trends and the nominal values presented in the technical specifications document of the Panasonic NCR18650B battery cell. On the other hand, the standard charging procedure starts with the constant current value, but when the specified voltage value is reached, the process continues with decreasing current values. This standard procedure is applied to extend the life of the battery. In the constant voltage region of the charging process, depending on decreasing current values, the natural convection cooling dominates the decreasing heat generation and the surface temperature is decreased as presented in Figure 6.

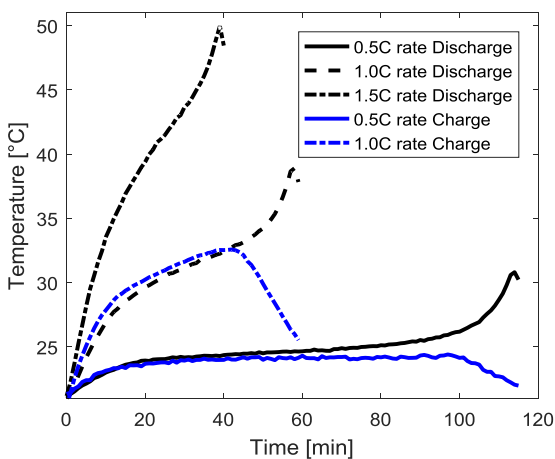


Figure 6. Surface temperature variation for different galvanostatic discharge/charge rates.

3.2. Battery Cell Behavior in a Driving Cycle

In order to tune the battery sub-model in vehicle

model, galvanostatic discharge/charge tests results were used. Battery sub-model internal resistance and open circuit voltage (OCV) were adjusted in a way to cover experimental voltage-time values.

After this adjustment, vehicle model was run in FTP-Highway driving cycle. Figure 7 shows the variation of the battery cell parameters in this driving cycle. According to the results, the battery current was bounded in permitted values and battery SoC (state of charge) was decreased about 15%. SoC value at the end of one cycle shows that this vehicle with specified parameters can repeat the driving cycle 5 times until depleting the battery cell capacity simultaneously.

Figure 8 shows the current-time values that were obtained by repeating the driving cycle 5 times. This time dependent current profile was chosen as input data for battery cell tests. The battery testing device was programmed to impose this profile on battery cells while their surface temperature was measured simultaneously.

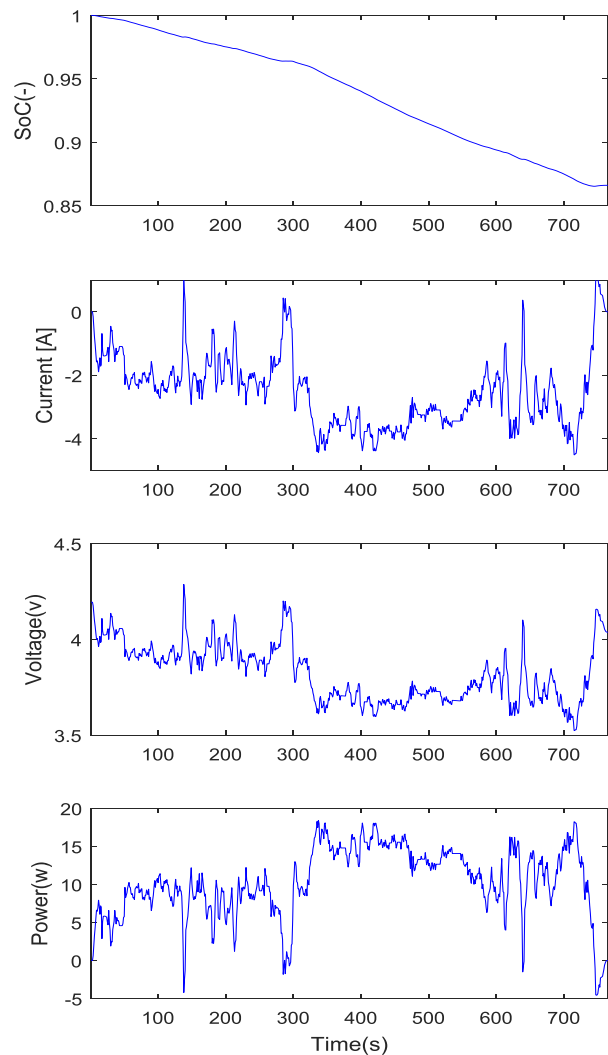


Figure 7. Battery cell parameters variation in FTP-highway driving cycle.

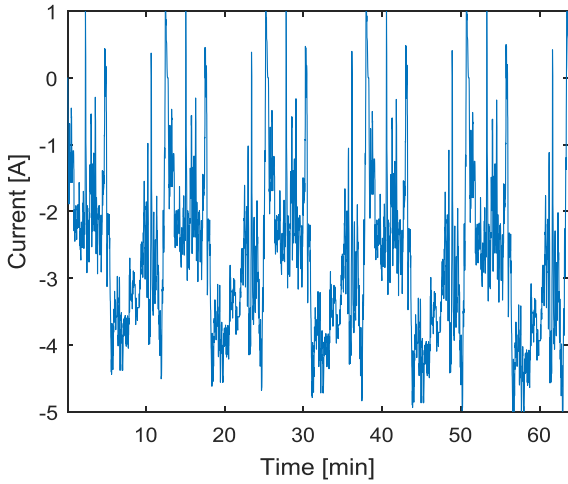


Figure 8. Current-time values implemented on battery cells.

A summary of ambient conditions is listed in Table 2. D1 case represents the room condition where the battery is exposed to ambient air. D2 and D3 represent the conditions with temperatures below and above the room temperature, respectively. In addition, D4 represents the experiments at which the battery cell was covered by insulation to provide a nearly adiabatic operating condition.

Table 2. Case studies conducted in this study.

Case Study	Ambient Temperature (°C)	Used Device
D1	20	Room
D2	-20, 0	Refrigerator
D3	40, 60	Oven
D4	-20, 20	Insulation

3.3. Battery Cell Thermal Behavior under Different Ambient Conditions

Figure 9 presents the battery surface and ambient temperature in D3 (40°C). Temperature variation shows an oscillatory behavior depending on the current input. The amplitude of these oscillations, which are characterized by increasing and decreasing battery surface temperature values, is approximately 2°C for the FTP-Highway driving cycle. In order to evaluate the case study results and the effects of applied driving cycle on the thermal behavior of the battery cell, the difference between the battery surface temperature and ambient temperature is shown in Figure 10(a). As can be seen from the figure, the temperature difference i.e., temperature rise of the battery, varies inversely with the ambient temperature. This means that in a cold environment, the battery cell tries to meet the same electrical requirements at the expense of generating more heat that is leading to higher surface temperature relative to the ambient.

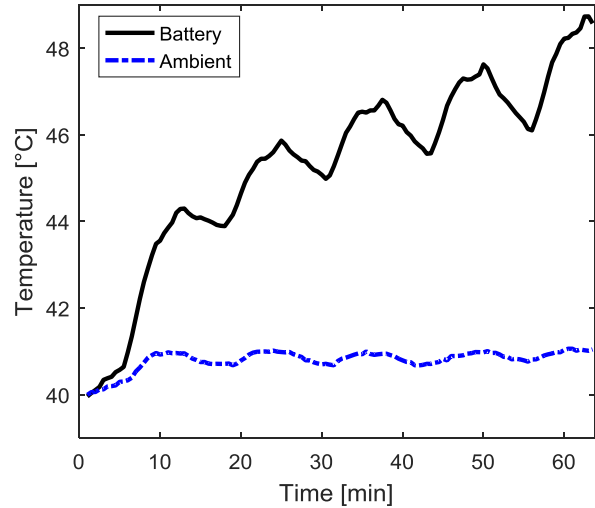


Figure 9. Battery surface temperature in FTP-Highway driving cycle (D3).

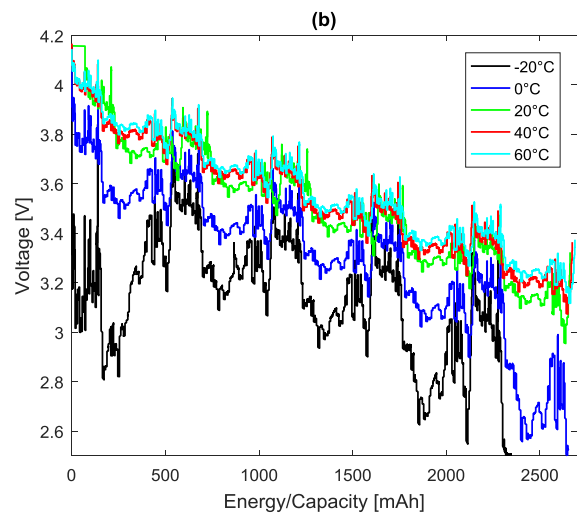
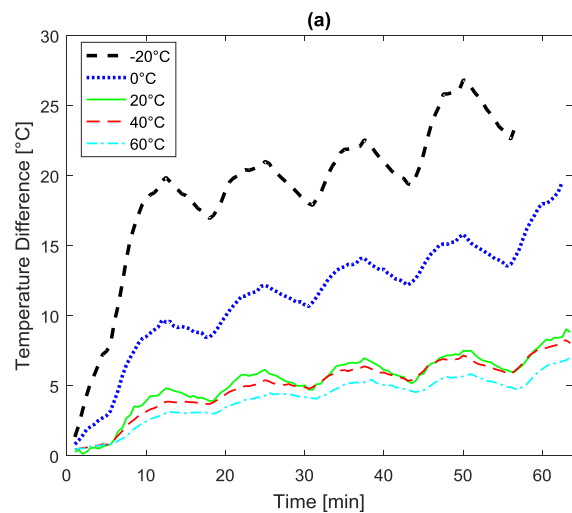


Figure 10. Battery behavior in FTP-highway driving cycle (D1, D2, D3) (a) surface temperature differences (b) voltage.

This is believed to be the result of increased internal resistance of the battery at low temperatures. The experimental results at -20 and 0°C operating temperatures show that there are 20°C and 10°C temperature differences after the first driving cycle respectively. However, the corresponding temperature rise is less than 5°C for the other operating conditions.

According to the variation of temperature data in Figure 10(a), the experiment with -20°C ambient temperature has been cut on 56th minute because the battery cell voltage has dropped below 2.5 V. The same cutoff limit has been reached for 0°C experiment at 63rd minute. On the other hand, all the other cases were able to complete the full five-cycle duration of 64 minutes without premature ending. Figure 10(b) presents the variation of battery capacity during experiments. The experiment with -20°C ambient temperature showed the lowest capacity (2345 mAh).

Among the battery thermal behavior tests, the highest temperature difference was observed in D4 case study. Figure 11 shows the battery surface temperature difference obtained under insulation. According to the results, a temperature difference of 46°C was experienced in D4 (-20°C) case, which is significantly higher than 30°C temperature difference obtained in D2 (-20°C). Therefore, the insulation magnifies the temperature difference as expected. It is also interesting to note that, early cutoff experienced with -20°C ambient temperature does not occur under the adiabatic-like conditions due to a large increase in the cell temperature as a result of insulation.

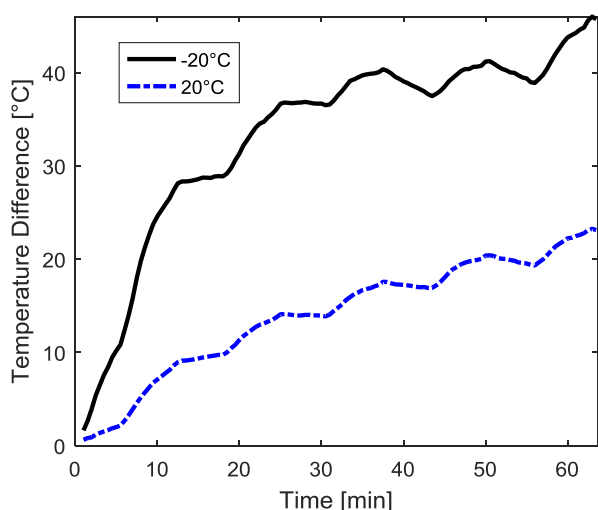


Figure 11. Battery surface temperature difference in FTP-highway driving cycle (D4).

4. Conclusions

In this paper, the thermal behavior of a Li-ion cell was examined under the FTP driving cycle at various

operating temperatures. The results show that the operating temperature has significant effects on the thermal performance of Li-ion batteries. It was found that the cold operating temperatures caused a significant increase in heat generation and surface temperature due to increasing internal resistance value of the cell.

Cold ambient conditions also lead to a severe decrement of the volumetric energy density and the capacity of the cell possibly due to weak ionic conductivity within the cell. Besides, it can be concluded from the given results that the difference between battery cell surface and ambient temperature is more pronounced as the ambient temperature decreases.

Acknowledgements

The authors would like to thank Scientific and Technological Research Council of Turkey (TÜBİTAK) for their support in the funding of this study (project no. 216M048).

References

- [1] Huo W., He H., Sun F., 2015. Electrochemical-thermal Modeling for a Ternary Lithium Ion Battery During Discharging and Driving Cycle Testing. *Royal Society of Chemistry Advancement*, **5**, pp. 57599-57607.
- [2] Pesaran A. A., 2002. Battery Thermal Models for Hybrid Vehicle Simulations. *Journal of Power Sources*, **110**, pp. 377-382.
- [3] Chung Y., Kim M. S., 2019. Thermal Analysis and Pack Level Design of Battery Thermal Management System with Liquid Cooling for Electric Vehicles. *Energy Conversion and Management*, **196**, pp. 105-116.
- [4] Motloch C., Christophersen J., Belt J., Wright R., 2002. High-power Battery Testing Procedures and Analytical Methodologies for HEV's. *SAE*, 797-802 doi: 10.4271/2002-01-1950.
- [5] Ramadas P., Haran B., White R., Popov B. N., 2002. Capacity Fade of Sony 18650 Cells Cycled at Elevated Temperatures: Part I Cycling Performance. *Journal of Power Sources*, **112**, pp. 606-613.
- [6] Bandhauer T. M., Garimella S., Fuller T. F., 2011. A Critical Review of Thermal Issues in Li-Ion Batteries. *Journal of the Electrochemical Society*, **158**, pp. 1-25.
- [7] Nagasubramanian G., 2001. Electrical Characteristics of 18650 Li-ion Cells at Low Temperatures. *Journal of Applied Electrochemistry*, **31**, pp. 99-104.

- [8] Jaguemont J., Boulon L., Dube Y., Poudrier D., 2014. Low Temperature Discharge Cycle Tests for a Li-Ion cell. Proceeding of IEEE Vehicle Power and Propulsion Conference, Coimbra, Portugal, 27-30 October, pp. 1-6.
- [9] Tourani A., White P., Ivey P., 2014. Analysis of Electric and Thermal Behavior of Lithium-ion Cells in Realistic Driving Cycles. Journal of Power Sources, **268**, pp. 301-314.
- [10] Panchal S., Mathew M., Dincer I., Agelin-Chaab M., Fraser R., Fowler M., 2018. Thermal and Electrical Performance Assessments of Lithium-ion Battery Modules for an Electric Vehicle under Actual Drive Cycles. Electric Power Systems Research, **163**, pp. 18-27.
- [11] Mastali M., Foreman E., Modjtahedi A., Samadani E., Amirfazli A., Fraser R. A., Fraser R. A., Fowler M., Farhad S., 2018. Electrochemical-thermal Modeling and Experimental Validation of Commercial Graphite/LiFePO₄ Pouch Lithium-ion Batteries, International Journal of Thermal Sciences, **129**, pp. 218-230.
- [12] Boyalı A., Güvenç L., 2010. Modeling and Rule Based Control of Hybrid Electric Vehicles. İTÜ Journal/D engineering, **9**, pp. 83-94.
- [13] EPA, 2019. Vehicle and Fuel Emissions Testing. United States Environmental Protection Agency, <https://www.epa.gov/vehicle-and-fuel-emissions-testing/vehicle-testing-regulations>. (Access Date: 01.01.2018).



Design, Analysis and Simulation of a 6-DOF Serial Manipulator

Zehranur YILMAZ^{1,*} , Orkun YILMAZ² , Zafer BİNGÜL³ 

¹ Department of Mechatronics Engineering, Kocaeli University, Kocaeli, 41310, Turkey, **ORCID:** 0000-0003-1930-6694

² Department of Mechatronics Engineering, Kocaeli University, Kocaeli, 41310, Turkey, **ORCID:** 0000-0003-1539-0905

³ Department of Mechatronics Engineering, Kocaeli University, Kocaeli, 41310, Turkey, **ORCID:** 0000-0002-9777-9203

Article Info

Research paper

Received : January 20, 2020

Accepted : May 31, 2020

Keywords

Dynamic Analysis
Jacobian
Kinematic Analysis
MATLAB/Simscape
PID Control
Trajectory Planning

Abstract

Within the scope of this study, firstly, the mechanical structure of a six-axis serial manipulator was designed. Forward kinematic analysis was made using the Denavit-Hartenberg method, which provides the transition between cartesian coordinates, that is, the linear and angular positions of the end-effector, and joint coordinates; joint angles and linear displacements. In addition, to obtain the relation between the speed of joint variables and the speed of end effector, Jacobian matrix was derived. Dynamic analysis of the system based on Lagrange-Euler mathematical model was acquired. After the design phase was carried out in three-dimensional environment, the physical system-based dynamic model was obtained by transferring this data to the MATLAB-Simscape environment. Inverse dynamic problem was solved to verificate the 3D design of robot and suitability of selected motors. To solve this problem, position, and velocity and acceleration trajectories was given to the dynamic model. As a result of this, each joint torques were obtained. The trajectories used in inverse dynamics were calculated using a fifth order polynomial function. Afterwards, in order to test the operation of the system in a simulated environment, PID based controller structures were applied to the dynamic model in MATLAB/Simulink simulation environment and forward dynamic problem was reviewed and discussed.

1. Introduction

With the increase in consumption in many areas in the 21st century, the production capacity has been increased and the use of autonomous systems that can work continuously with high efficiency without getting tired is becoming widespread. Robots come first among the autonomous systems since they have the ability to perform various tasks. For this reason, the development of robots for use in the industry in our country can be described as an important technological step in the country's rise to the level of developed countries. The purpose of this study is to create a substructure to overcome this deficiency. In robot technology, many control methods are used to provide very precise and stable working cycles.

At the point of control of serial robots, PID based control methods [1] as well as many nonlinear control methods are also used [2-3]. Likewise, in [4] and [5],

control of the robot was carried out using evolutionary algorithms (PSO). It is a common approach to benefit from mathematical models when using these control methods. When performing dynamic analysis of robots, energy-based models such as Lagrange-Euler [6-10] or force-based models such as Newton-Euler [11] occupy a wide range in the literature. Whether the model created during the use of mathematical models fully meets the system is a very important criterion [12]. Although a mathematical model prepared by neglecting inputs such as real-time friction and actuator dynamics into the control system and dynamic analysis based on this model seems to be an ideal system in the simulation environment, it is far from real time. Modeling of a robot designed in three-dimensional environment through Simscape in Simulink environment has been adopted as an effective approach to obtain the physical component and physical connection data of the robot very close to real time. Simscape based modeling has many uses; PV generators in microgrid scenario [13], power PIN diodes [14], wind turbine gearboxes [15], 3-RPS

* Corresponding Author: ylmz.zehranur@gmail.com



parallel robotics [16], 5-DOF robotic manipulators [17]. All body components and materials of the robot were selected according to the calculations made during the design phase. Forward and inverse kinematics problems, which provide the transition between cartesian coordinates, that is, the linear and angular positions of the gripper, and joint coordinates, i.e. joint angles and displacements are discussed. Forward and inverse kinematics problems that provide the transition between the Cartesian coordinates that is the linear and angular positions of the end effector, and joint coordinates, i.e. joint angles and joint displacements are discussed. Kinematic, Jacobian and dynamic analysis are given in Section 2. In Section 3, simulation results are shown. Finally, conclusion is shared in Section 4.

2. Materials and Methods

In this study, 6-DOF serial manipulator ZORO-1 was developed to be remotely controlled by a human that can fulfill tasks such as pick and place. As a result of this, ZORO-1 was designed based on the human arm and all of its joints were selected as revolute joints. Robot's 3D structure was modeled in Autodesk Inventor program which is shown in Figure 1.

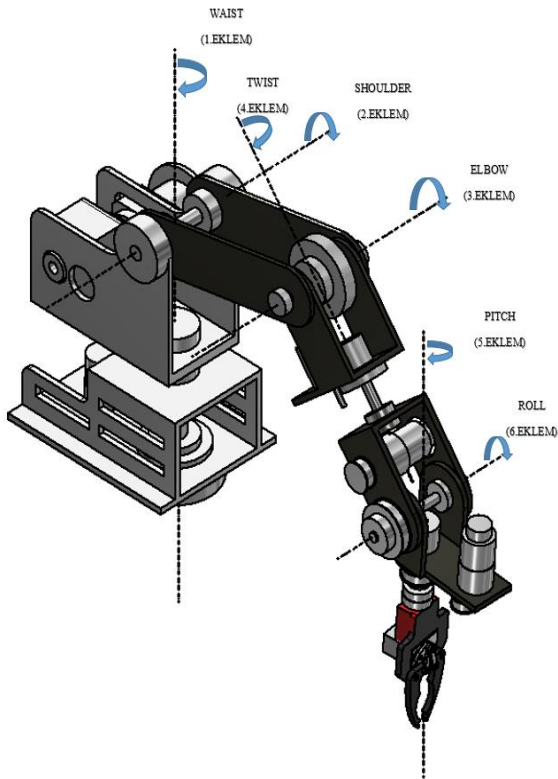


Figure 1. Mechanical structure of ZORO-1.

In the subsections below, the kinematic and dynamic model of ZORO-1 is presented. Evaluation of your work or to repeat the experiments exactly as you have done them.

2.1. Kinematic Analysis

In this study, Denavit-Hartenberg (DH) method was used to obtain the kinematic model of ZORO-1 robot. With DH method, the end effector's position and orientation data according to reference coordinate frame can be calculated parametrically in terms of joint variables. As the first step, cartesian coordinat frames were placed (Figure 2). Then the DH parameters of the robot were found and are shown in Table 1.

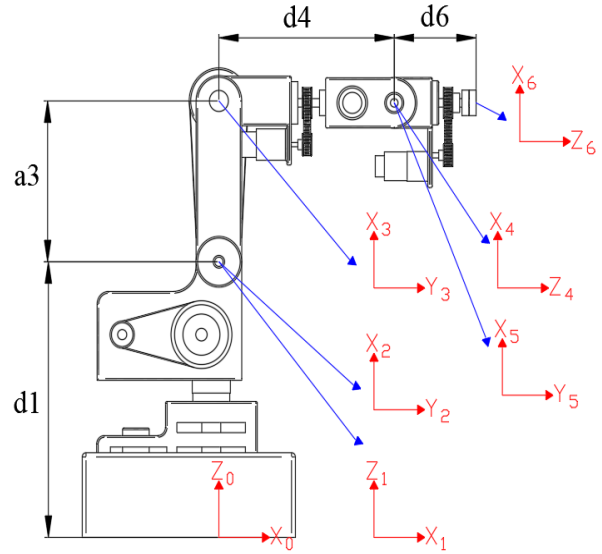


Figure 2. Cartesian coordinate frames of the robot.

Table 1. DH parameters of ZORO-1.

i	α_i (deg)	a_i (m)	d_i (m)	θ_i (deg)
1	$\alpha_1 = 0$	$a_1 = 0$	$d_1 = 0.32$	θ_1
2	$\alpha_2 = -90$	$a_2 = 0$	$d_2 = 0$	$\theta_2 - 90$
3	$\alpha_3 = 0$	$a_3 = 0.19$	$d_3 = 0$	θ_3
4	$\alpha_4 = -90$	$a_2 = 0$	$d_4 = 0.23$	θ_4
5	$\alpha_5 = 90$	$a_2 = 0$	$d_5 = 0$	θ_5
6	$\alpha_6 = -90$	$a_2 = 0$	$d_6 = 0.11$	θ_6

Secondly, forward kinematic transformation matrices were derived using DH parameters in Eq. (1).

$${}^0_1T = \begin{bmatrix} c_1 & -s_1 & 0 & 0 \\ s_1 & c_1 & 0 & 0 \\ 0 & 0 & 1 & d_1 \\ 0 & 0 & 0 & 1 \end{bmatrix}, \quad {}^1_2T = \begin{bmatrix} s_2 & c_2 & 0 & 0 \\ 0 & 0 & 1 & 0 \\ c_2 & -s_2 & 0 & 0 \\ 0 & 0 & 0 & 1 \end{bmatrix},$$

$${}^2_3T = \begin{bmatrix} c_3 & -s_3 & 0 & a_3 \\ -s_3 & -c_3 & 0 & 0 \\ 0 & 0 & 1 & 0 \\ 0 & 0 & 0 & 1 \end{bmatrix}, \quad {}^3_4T = \begin{bmatrix} c_4 & -s_4 & 0 & 0 \\ 0 & 0 & 1 & d_4 \\ -s_4 & -c_4 & 0 & 0 \\ 0 & 0 & 0 & 1 \end{bmatrix}, \quad (1)$$

$${}^4_5T = \begin{bmatrix} c_5 & -s_5 & 0 & 0 \\ 0 & 0 & -1 & 0 \\ s_5 & c_5 & 0 & 0 \\ 0 & 0 & 0 & 1 \end{bmatrix}, \quad {}^5_6T = \begin{bmatrix} c_6 & -s_6 & 0 & 0 \\ 0 & 0 & 1 & d_6 \\ -s_6 & c_6 & 0 & 0 \\ 0 & 0 & 0 & 1 \end{bmatrix}$$

where s_i and c_i represent $\sin \theta_i$ and $\cos \theta_i$ respectively. To calculate the transformation matrix 0_6T was used in Eq. (2):

$${}^0_6T = {}^0_1T {}^1_2T {}^2_3T {}^3_4T {}^4_5T {}^5_6T \quad (2)$$

In Eq. (3) all row and column of 0_6T matrix elements were demonstrated:

$${}^0_6T(1,1) = -c_1s_{23}s_4s_6 + s_1c_4s_6 + s_1s_4c_5c_6 + c_1s_{23}c_4c_5c_6 + c_1c_{23}s_5c_6$$

$${}^0_6T(2,1) = -c_1c_4s_6 - s_1s_{23}s_4s_6 - c_1s_4c_5c_6 + s_1s_{23}c_4c_6 + s_1c_{23}s_3c_6$$

$${}^0_6T(3,1) = c_{23}c_4c_5c_6 - s_{23}s_5s_6 - c_{23}s_4s_6$$

$${}^0_6T(1,2) = -s_1c_4c_6 - c_1s_{23}s_4c_6 - s_1s_4c_5s_6 - c_1s_{23}c_4c_5s_6 - c_1c_{23}s_5s_6$$

$${}^0_6T(2,2) = c_1s_4c_5s_6 - s_1s_{23}c_4s_6 - s_1c_{23}s_5 - c_1c_4c_6 - s_1s_{23}s_4c_6 - c_1c_4c_6$$

$${}^0_6T(3,2) = s_{23}s_5s_6 - c_{23}c_4c_5s_6 - c_{23}s_4c_6 \quad (3)$$

$${}^0_6T(1,3) = -c_1c_{23}c_5 - s_1s_4s_5 - c_1s_{23}c_4s_5$$

$${}^0_6T(2,3) = c_1s_4s_5 - s_1s_{23}c_4s_5 - s_1c_{23}c_5$$

$${}^0_6T(3,3) = -s_{23}c_5 - c_{23}c_4s_5$$

$${}^0_6T(1,4) = a_3c_1s_2 + d_4c_1c_{23} - d_6(s_1s_4s_5 + c_1s_{23}c_4s_5 - c_1c_{23}c_5)$$

$${}^0_6T(2,4) = a_3s_1s_2 + d_4s_1c_{23} + d_6(c_1s_4s_5 - s_1s_{23}c_4s_5)$$

$${}^0_6T(3,4) = d_1 + a_3c_2 - d_4s_{23} - d_6(s_{23}c_5 + c_{23}c_4s_5)$$

where s_{ij} and c_{ij} represent $\sin(\theta_i + \theta_j)$ and $\cos(\theta_i + \theta_j)$ respectively.

2.2. Jacobian Analysis

The Jacobian matrix provides the transition between the velocity of the joint variables and the linear and angular velocities of the end effector. The dimension of this matrix is $6 \times n$, where n represents the number of joint variables. While J_v , which constitutes the first three lines and relates to linear velocities, was calculated by the direct derivations of the position vectors, last three lines J_ω ,

which relates to angular velocities, was taken from the relevant part in the rotation matrices in Eq. (4), Eq. (5), and Eq. (6);

$$J = \begin{bmatrix} J_v \\ J_\omega \end{bmatrix} \quad (4)$$

$$J_v = \begin{bmatrix} \frac{\partial p_x}{\partial q_1} & \frac{\partial p_x}{\partial q_2} & \frac{\partial p_x}{\partial q_{n-1}} & \frac{\partial p_x}{\partial q_n} \\ \frac{\partial p_y}{\partial q_1} & \frac{\partial p_y}{\partial q_2} & \frac{\partial p_y}{\partial q_{n-1}} & \frac{\partial p_y}{\partial q_n} \\ \frac{\partial p_z}{\partial q_1} & \frac{\partial p_z}{\partial q_2} & \frac{\partial p_z}{\partial q_{n-1}} & \frac{\partial p_z}{\partial q_n} \end{bmatrix} \quad (5)$$

$$J_\omega = \begin{bmatrix} {}^0R\hat{Z}_1\xi_1 & {}^0R\hat{Z}_2\xi_2 & \dots & {}^0R\hat{Z}_{n-1}\xi_{n-1} & {}^0R\hat{Z}_n\xi_n \end{bmatrix} \quad (6)$$

The rotational and translational Jacobian matrices were obtained as;

where \hat{Z}_i is $[0 \ 0 \ 1]^T$ vector and ξ_i is a coefficient which indicates the joint type and for rotational joints it's "1", for prismatic joints it's "0". The relationship between joint space and cartesian space speeds can be given as Eq. (7):

$$\dot{x} = J\dot{q} \quad (7)$$

$$\text{where } \dot{x} = \begin{bmatrix} \dot{u}_x \\ \dot{u}_y \\ \dot{u}_z \\ \dot{\omega}_x \\ \dot{\omega}_y \\ \dot{\omega}_z \end{bmatrix}, \quad \dot{q} = \begin{bmatrix} \dot{q}_1 \\ \dot{q}_2 \\ \vdots \\ \dot{q}_{n-1} \\ \dot{q}_n \end{bmatrix}$$

2.3. Dynamic Analysis

In this subsection, the dynamic model of ZORO-1 robot is discussed. Dynamics is the field of science that studies the motions of objects under a cause and effect relationship with the forces applied to them. In this study, Lagrange-Euler equations were used to obtain the dynamic model. This method is an energy-based approach. Firstly, Lagrangian (L) must be found using the total kinetic (K) and potential (P) energies of the system Eq. (8).

$$L(q, \dot{q}) = K(q, \dot{q}) - P(q) \quad (8)$$

Thus, the equations of the motion could be obtained as in Eq. (7);

$$\frac{d}{dt} \left(\frac{\partial L}{\partial \dot{q}} \right) - \frac{\partial L}{\partial q} = \tau \quad (9)$$

where q and τ are joint variables and torques respectively.

By using Eq. (9) the general robotic dynamic equation can be derived as in Eq. (10);

$$D(q)\ddot{q} + C(q,\dot{q}) + G(q) = \tau \quad (10)$$

while D is the mass matrix which contains the inertial forces, C is the coriolis vector. G is the gravity vector which hosts the gravitational forces.

The total kinetic energy of a system can be given as follows;

$$K(q,\dot{q}) = \frac{1}{2} \sum_{i=1}^n (V_i)^T m_i V_i + (\omega_i)^T I_i \omega_i \quad (11)$$

In Eq. (11), m_i and I_i are the mass and inertia matrix of i-th link respectively. Cartesian velocities can be written in terms of joint velocities by using Jacobian as follows;

$$V_i = J_v \dot{q}, \quad \omega_i = J_\omega \dot{q} \quad (12)$$

Substituting Eq. (12) into Eq. (11) yields;

$$K(q,\dot{q}) = \frac{1}{2} \dot{q}^T \sum_{i=1}^n \left[(J_{v_i})^T m_i J_{v_i} + (J_{\omega_i})^T I_i J_{\omega_i} \right] \dot{q} \quad (13)$$

In this equation, the part in brackets is the mass matrix. By using the below Eqs. (14-15) coriolis vector in Eq. (16) can be obtained from mass matrix;

$$D(q) = \left[(J_{v_i})^T m_i J_{v_i} + (J_{\omega_i})^T I_i J_{\omega_i} \right] \quad (14)$$

$$C(q,\dot{q}) = \sum_{k=1}^n \sum_{j=1}^n \left[c_{kj}^i(q) \dot{q}_k \dot{q}_j \right] \quad (15)$$

$$c_{kj}^i(q) = \frac{\partial}{\partial \dot{q}_k} D_{ij}(q) - \frac{1}{2} \frac{\partial}{\partial \dot{q}_i} D_{kj}(q), \quad 1 \leq i, j, k \leq n \quad (16)$$

And finally G vector can be derived by Eq. (17);

$$G(q) = - \sum_{k=1}^n \sum_{j=1}^n \left[g_k m_j A_{ki}^j(q) \right] \quad (17)$$

Gravity matrix elements were given in Eqs. (18-22);

$$G(1) = 0 \quad (18)$$

$$G(2) = \frac{1}{2} g \left(\frac{m_5}{200} (c_{23} d_4 + a_3 s_2 + d_6 c_{23} s_5 + d_6 s_{23} c_4 c_5) + m_4 \left(d_4 c_{23} - \frac{9}{200} c_{23} + a_3 s_2 \right) + m_3 \left(\frac{9}{200} c_{23} + a_3 s_2 \right) + \left(\frac{1}{2} a_3 m_2 s_2 \right) \right) \quad (19)$$

$$G(3) = g \left(\frac{9}{200} m_3 c_{23} d_4 + m_5 d_4 c_{23} + \frac{1}{2} d_6 (c_{23} s_5 + s_{23} c_4 c_5) - m_4 \left(\frac{9}{200} c_{23} d_4 + d_4 c_{23} \right) \right) \quad (20)$$

$$G(4) = \frac{1}{2} g m_5 d_6 c_{23} s_4 c_5 \quad (21)$$

$$G(5) = \frac{1}{2} g m_5 d_6 (s_{23} c_5 + c_{23} c_4 s_5) \quad (22)$$

The inertial parameters of ZORO-1 robot which were taken from Inventor program are shown in Figure 3. These parameters were used to obtain the simulation results in MATLAB/Simulink.

First, inverse dynamics problem was discussed. In this problem, joint torques can be calculated by giving trajectories of position, velocity and acceleration of all joints to dynamic model. Inverse dynamic analysis is used for verification of mechanical model and motor selection.

Forward dynamics analysis was made to simulate ZORO-1 robot. To control the robot a PID controller was created and adapted to dynamic model. Both forward and inverse dynamics simulation results are given in Section 3.

2.4. Trajectory Planning

In this study, for achieving the solution of inverse dynamics trajectory planning has been made. A fifth order polynomial was used in position trajectory which is given below;

$$\theta(t) = s_0 + s_1 t + s_2 t^2 + s_3 t^3 + s_4 t^4 + s_5 t^5 \quad (23)$$

$$\dot{\theta}(t) = s_1 + 2s_2 t + 3s_3 t^2 + 4s_4 t^3 + 5s_5 t^4 \quad (24)$$

$$\ddot{\theta}(t) = 2s_2 + 6s_3 t + 12s_4 t^2 + 20s_5 t^3 \quad (25)$$

where;

$$s_0 = \theta_0, \quad s_1 = \dot{\theta}_0,$$

$$s_3 = \frac{20(\theta_f - \theta_0) - (8\dot{\theta}_f + 12\dot{\theta}_0)t_f + (\ddot{\theta}_f - 3\ddot{\theta}_0)t_f^2}{2t_f^3},$$

$$s_4 = \frac{30(\dot{\theta}_f - \dot{\theta}_0) + (14\ddot{\theta}_f + 16\ddot{\theta}_0)t_f + (3\ddot{\theta}_f - 2\ddot{\theta}_0)t_f^2}{2t_f^4},$$

$$s_5 = \frac{12(\ddot{\theta}_f - \ddot{\theta}_0) - 6(\dot{\theta}_f - \dot{\theta}_0)t_f - (\ddot{\theta}_f - \ddot{\theta}_0)t_f^2}{2t_f^5}.$$

Center of mass expressed in base coordinate frame/(m)			Moment of inertial for center of mass and expressed in center of mass coordinate frame/(kg· m ²)									Part mass/kg	Moving Part Number	Moving part of ZORO-1 robot designed by Inventor
x	y	z	I _{xx}	I _{xy}	I _{xz}	I _{yx}	I _{yy}	I _{yz}	I _{zx}	I _{zy}	I _{zz}			
-0.01	0.03	0	0.03	0.001	0.001	0.001	0.01	-0.003	0.001	-0.003	0.026	3.78	Part1	
0	0	0.02	0.003	0	0	0	0.003	0	0	0	0.0008	0.52	Part2	
0.008	0.056	-0.001	0.0017	-0.0003	0	-0.0003	0.001	0	0	0	0.002	0.84	Part3	
0	-0.017	0.04	0.0005	0	0	0	0.0002	0	0	0	0.0004	0.24	Part4	
-0.02	0.003	0.03	0.0007	0	0	0	0.0012	0	0	0	0.0012	0.62	Part5	
0	0	0.017	0	0	0	0	0	0	0	0	0	0.066	Part6	

Figure 3. Inertia tensor elements and masses of moving part of ZORO-1 robot.

3. Simulation Results

In this study, two dynamic problems were solved for ZORO-1 robot.

3.1. Inverse Dynamic Problem

First of all, to solve the inverse dynamics problem, position, velocity and acceleration trajectories of all joints were given to the dynamic model and as a result of this joint torques were calculated. This analysis was done for verification of 3D model of robot and motor selection. The trajectories are given in Figures 4-6, respectively.

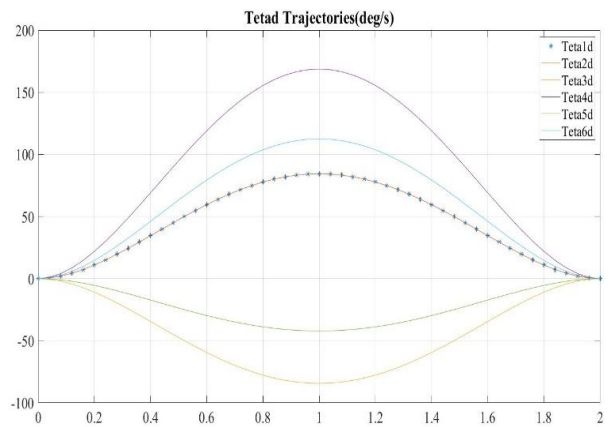


Figure 5. Velocity trajectories.

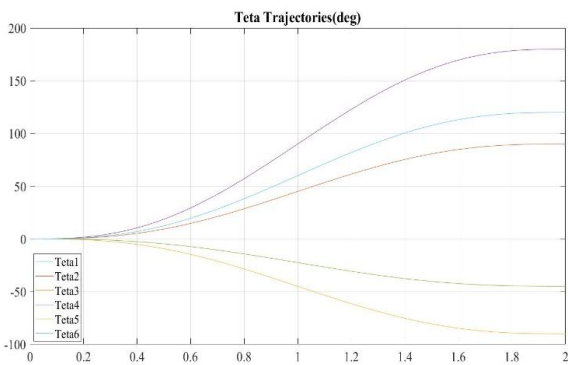


Figure 4. Position trajectories.

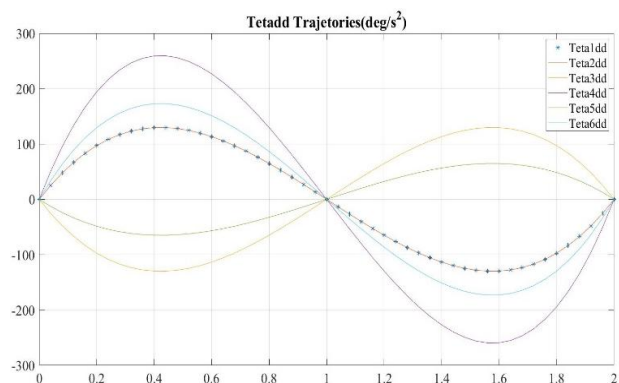


Figure 6. Acceleration trajectories.

Calculated torques for each joint for given trajectories are also given in Figure 7.

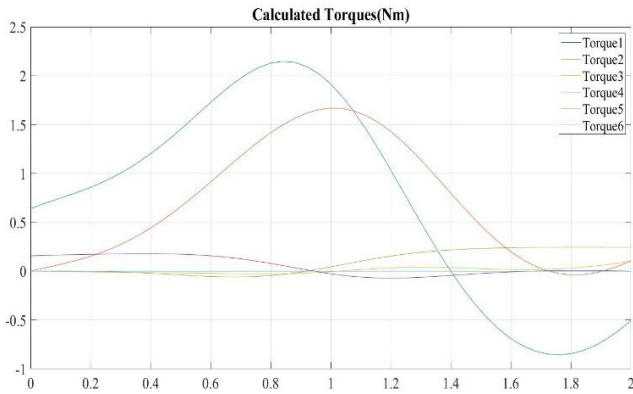


Figure 7. Calculated torques.

After results were viewed, mechanical model and selected motors were verified.

3.2. Forward Dynamic Results

In this subsection, a PID based controller was created and connected to dynamic model. For controlling the joint variables a simulation was developed. In Figure 8, joint variables-time graphs were shown via their reference signals and the controller signals are given in Figure 9.

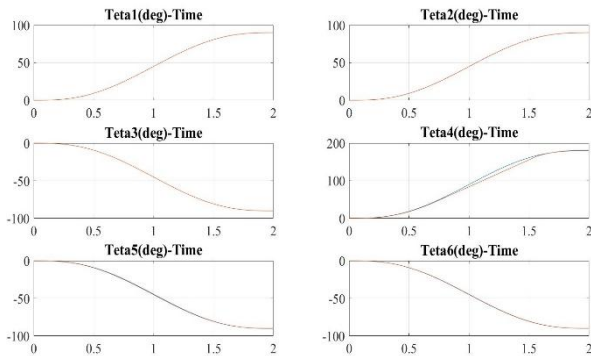


Figure 8. Joint variables-time graphics.

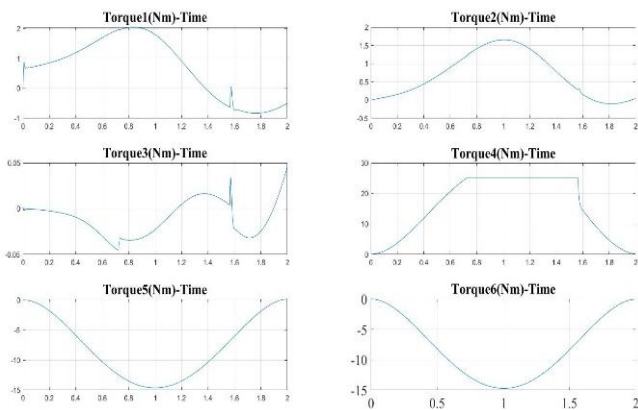


Figure 9. Controller signals in Simscape simulation.

Desired trajectory tracing for ZORO-1 robot was achieved with developed PID controller with considering limitations in motor torques.

4. Conclusions

In this article, firstly, the mechanical design of the ZORO-1 robot was realized. Since the robot developed in future studies will be focused on remote control with a Human-Machine Interface (HMI), the human arm is taken as the design stage of the robot in order to avoid any problems in compatibility. Kinematic, dynamic and Jacobian analyses of the developed robot were made. As a result of these studies, the system was transferred to the MATLAB-Simscape environment. The suitability of the 3D design and actuators of the robot developed in the first stage was evaluated. For this, the inverse dynamic problem is dealt with in the MATLAB-Simulink environment. The system has been verified because the torque values calculated in this direction can be provided by the motors actually selected. In the following stage, a PID based controller has been developed and adapted to this dynamic model and the system has been simulated in MATLAB-Simulink environment. It was determined that the desired control was achieved as a result of the simulation.

References

- [1] Zhang D., Wei B., 2016. Design of a Joint Control System for Serial Mechanical Arms Based on PID and MRAC Control. Asia-Pacific Conference on Intelligent Robot System, Tokyo, Japan, 20-22 July, pp. 91-96.
- [2] Katliar M., Drop F. M., Teufel H., Diehl M., Bulthoff H. H., 2018. Real-Time Nonlinear Model Predictive Control of a Motion Simulator. 2018 European Control Conference (ECC), Limassol, South Cyprus, 12-15 June, doi: 10.23919/ECC.2018.8550041.
- [3] Bingül Z., Karahan O., 2012. Fractional PID Controllers Tuned by Evolutionary Algorithms for Robot Trajectory Control. Turkish Journal of Electrical Engineering & Computer Sciences, 20(Sup.1), 1123-1136.
- [4] Bingül Z., Karahan O., 2011. A Fuzzy Logic Controller Tuned with PSO for 2 DOF Robot Trajectory Control. Expert Systems with Applications, doi: 10.1016/j.eswa.2010.07.131.
- [5] Bingül Z., Varol H. A., 2004. A New PID Tuning Technique Using Ant Algorithm. Proceeding of the 2004 American Control Conference, Boston, Massachusetts, 30 June – 2 July.

- [6] Angeles J., 2007. Fundamentals of Robotic Mechanical Systems, Methods and Algorithms. Springer Science+Business Media LLC, 3rd ed., New York, NY, USA. Robotic Manipulator for Direct Additive Manufacturing on the Internal Surface of Radome Systems. The International Journal of Advanced Manufacturing Technology, **101**(5-8), pp. 2027-2036.
- [7] Murray R. M, Li Z., Sastry S. S., 1994. A Mathematical Introduction to Robotic Manipulation, Berkeley: CRC Press, University of California.
- [8] Dombre E., Khalil W., 2007. Modeling, Performance Analysis and Control of Robot Manipulators, ISTE Ltd., London, UK.
- [9] Sciavicco L., Siciliano B., 2000. Modelling and Control of Robot Manipulators, Springer, London, UK.
- [10] Siciliano B., Sciavicco L., Villani L., Oriolo G., 2009. Robotics: Modelling, Planning and Control, Springer, London, UK.
- [11] Kunquan L., Rui W., 2011. Closed-form Dynamic Equations of 6-RSS Parallel Mechanism Through the Newton-Euler Approach. Third International Conference on Measuring Technology and Mechatronics Automation, Henan Engineering Institute, Zhengzhou, China, 6-7 January, pp. 712-715.
- [12] Wikipedians, 2019. Mathematical model, Wikipedia, https://en.wikipedia.org/wiki/Mathematical_model. (Access Date: 02 December 2019).
- [13] Basak P., Chowdhury S., Chowdhury S. P., 2013. Simscape Based Modeling and Simulation of a PV Generator in Microgrid Scenario. 22nd International Conference and Exhibition on Electricity Distribution (CIRED), Stockholm, Sweden, 10-13 June, paper no: 0997.
- [14] Elwarraki E., Mijlad N., Elbacha A., 2016. SIMSCAPE Electro-thermal Modelling of the PIN Diode for Power Circuits Simulation. IET Power Electronics, **9**(7), pp. 1521-1526.
- [15] Al-Hamadani H., An T., King M., Long H., 2017. System Dynamic Modelling of Three Different Wind Turbine Gearbox Designs Under Transient Loading Conditions. International Journal of Precision Engineering and Manufacturing, **18**(11), pp. 1659-1668.
- [16] Olaya J., Pintor N., Avilés O. F., Chaparro J., Analysis of 3 RPS Robotic Platform Motion in Simscape and MATLAB GUI Environment. International Journal of Applied Engineering Research, **12**(8), pp. 1460-1468.
- [17] Grazioso S., Di Maio M., Di Gironimo G., 2019. Conceptual Design, Control, and Simulation of a 5-DoF



Turbulence Modelling on Fluidized Bed Gasification

Ebubekir BEYAZOGLU^{1,*} Erhan PULAT²

¹ Department of Mechanical Engineering, Bursa Uludag University, Bursa, 16059, Turkey, **ORCID:** 0000-0002-7327-8471

² Department of Mechanical Engineering, Bursa Uludag University, Bursa, 16059, Turkey, **ORCID:** 0000-0003-2866-6093

Article Info

Research paper

Received : January 14, 2020

Accepted : July 21, 2020

Keywords

Computational Fluid Dynamics (CFD)

Combustion

Gasification

Solid Waste Material

Turbulence

Waste Management

Abstract

Energy generation from carbon-based solid materials, such as coal by a gasification process, increasingly has become an essential research subject, as current energy sources are getting to an end. Waste material management is also of considerable significance to dispose of them sustainably and efficiently from the environment. There is, therefore, the need for an advanced modeling approach to maximize the efficiency of coal-derived synthesis gas, and to optimize process parameters for designing a new gasifier. Hence, a two-dimensional (2-D) gasification system was initially simulated by using commercial code ANSYS FLUENT. Devolatilization and char combustion chemical reactions of the process were modeled by User Defined Functions (UDF) to simulate their chemical kinetics more accurately. Once a mesh independency study was fulfilled, performance evaluation was done, and the energy efficiency of the gasification system was also calculated. Subsequently, model validation has been performed, and RANS based turbulence models were examined to find out the best turbulence modeling approach.

1. Introduction

The solid waste is drastically increasing as a dominant pollution issue all around the world. This waste has been disposed to landfill enormously, and most of them have remained a dangerous waste for the ecology, as well as human health. For instance, roughly 55 million tons of post-consumer solid waste is produced by the Far East, Europe, and the USA [1]. Solid waste decreasing, energy generation and clean-burning gas are the main realities to address the attraction of the process. On the other hand, the process is very complicated to visualize, and to explain scientific concepts of the system, such as solid particles, are the real problem associated with combustion. Complete oxidation is hard for solid fuels, and particulate matter is a real problem. For this reason, it is a necessity to develop a simple, reliable, and accurate model for engineering and scientific calculations. In recent years, high-temperature process phenomena such as pyrolysis, combustion, or

gasification, as shown in Figure 1, have gained an increased interest in developing more new models for better use of solid waste with regard to regenerating renewable energy [2].

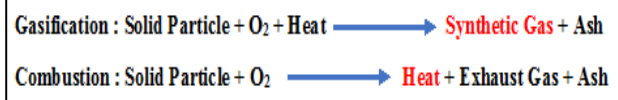


Figure 1. Schematic of chemical reactions for gasification and combustion processes.

Gasification is a gas generation process, which is operated at high temperatures around (600°C to 800°C) to react materials without combustion, with a controlled amount of oxygen and/or steam. The process converts organic or fossil fuel-based carbonized materials into carbon monoxide, hydrogen, or carbon dioxide using sequentially occurring chemical reactions, and those output mixture gases are generally called Syngas or Synthetic Natural Gas [3]. Upon generation of the synthetic gas, it is converted to mechanical work, heat, or electricity as a different type of energy for the market demand. Combustion is a thermo-chemical process but produces

* Corresponding Author: ebeyazoglu@uludag.edu.tr

This article is an extended version of the paper presented at the 22nd Congress on Thermal Science and Technology.



thermal energy without any synthetic gas generation. Pyrolysis is also a similar process like gasification and combustion; it is initially generated bio-oils, and these are finally converted to chemical fuels, like hydrogen. The following literature review is conducted regarding gasification and combustion research.

Gunarathne et al. [4] have studied on pretreatment of biomass, and this method is continuously increasing due to the high demand for it and retaining low energy density. They have used steam-blown black pellets and unpretreated gray pellets to gasify with air and steam at an updraft high-temperature agent gasification unit. Horton et al. [5] developed a CFD model to simulate a solid waste gasification process using the Fluent commercial code. For this study, the Kinetic Modeling Editor (K.M.E.) was coupled to a Computational Fluid Dynamics (CFD) solver to allow equipment level information into the design. High-temperature air combustion (HiTAC) has been numerically analyzed. HiTAC would be a promising advanced technology for heat regaining, energy-conserving, and stability enhancement of flame. Pour et al. [6] developed a CFD model, which is known as an applied tool to perform (HiTAC) modeling. Zhou et al. [7], worked on steam gasification of municipal solid waste (MSW) using a CaO additive. They used a batch-type fixed bed reactor to investigate the effects of CaO addition on heat transfer properties. Li et al. [8], devolatilized biomass at high temperatures and high heating rates. Biomass reactivity was lowered and allowed greater torrefaction conducted after torrefaction. The kinetic parameters of torrefied biomass were also calculated. CO and H₂ were the primary vaporizing volatiles during the devolatilization of torrefied biomass. The effects of the product yields and composition of the biomass formed during steam pyrolysis were investigated on the metal modified HZSM 5 to the zeolite/binder ratio (Z/B). Catalytic steam pyrolysis of biomass was researched in a bubbling fluidized bed reactor at 450°. The effects of silica-supported transition metals (Ni and V) on product yields and compositions were investigated in [9]. A new solution method for biomass pyrolysis was generated. An advanced 3-D kinetic model was developed for biomass pyrolysis coupled with CFD in this study. Although their simulations were very time consuming, Mellin et al. [10] made it possible to investigate secondary reactions in the biomass pyrolysis. Gunarathne et al. [11] developed an equation for pressure drop divination with a compression influence and presented graphical representations of correlation constants. They also provided a lead to delineate pellet size and designing a grate. Schulze et al. [12] performed a very predictive and novel char particle gasification study to determine the carbon conversion rate for the efficient gasifier. The focus of their research is to develop an

alternative advanced model to maximize the efficiency of the gasification process for designing a new gasifier. Calculation of design variables, optimization of them, stable waste properties, and also determining processing conditions are the second most essential calculations of this study.

As the above literature review illustrates the key features of the gasification process, this research is mainly involved in a set of physical conversions and chemical reactions. It consists of moisture release, devolatilization, tar cracking, and char combustion, as shown in Figure 2.

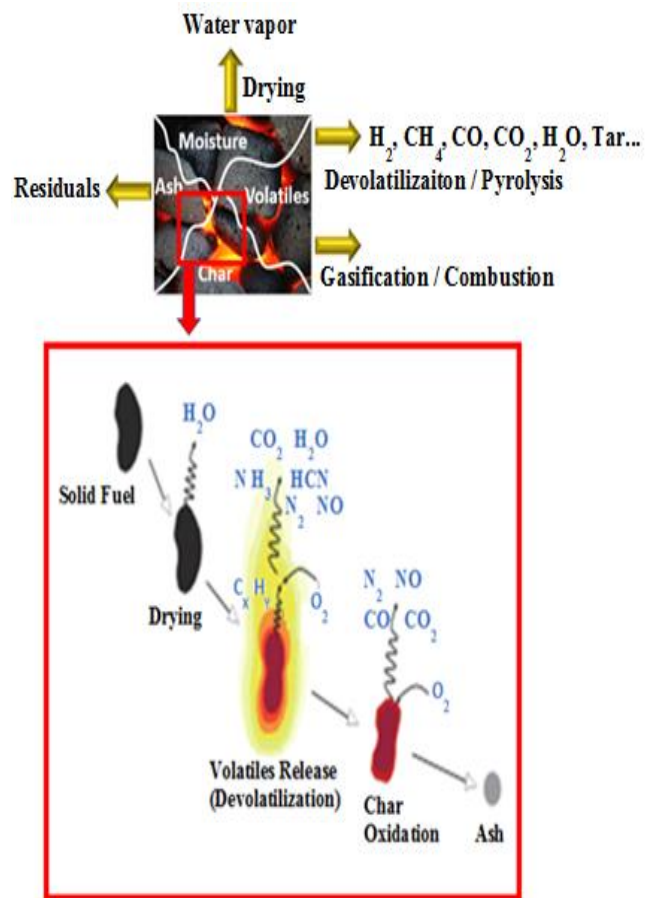


Figure 2. Solid fuel combustion and gasification [13].

As it is mentioned, the gasification is a highly complex thermochemical process, and gasification modeling of solid waste particles is relatively limited in the literature. Hence, in this study, systematic investigation of solid waste as a syngas generation and also understanding the transport phenomena with its chemical reaction mechanisms during the process are of primary interest. The primary purpose of this research is, therefore, to study the gasification of solid waste on particle transport, momentum, heat, and mass transfer. A 2-D multiphase reacting flow model was developed. This developed CFD model may have a significant impact on gasifier design,

process optimization, and it would also be used as a research tool.

2. Materials and Methods

The place of gasifier in the complete set of solid waste gasification and energy generation processes is given in Figure 3. There are different types of gasifiers used for gasification processes such as the Cyclone Gasifier (CG), Dwindraft Bioamas Gasifier (DBG), Entrained Flow Gasifier (EFG), and Fluidized Bed Gasifier (FBG), and brief review of biomass gasification modeling can be found in [14].

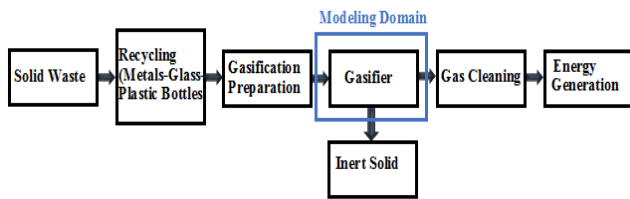


Figure 3. Schematic of solid waste gasification and energy generation.

The main product of the gasification process is the Syngas, i.e., relatively environmentally friendly and energy-efficient gas, which contains carbon monoxide, hydrogen, and methane. The other product is solid leftover, which consists of non-combustible materials (ash) and includes a relatively low level of carbon. Syngas can be used in different ways; for example, Syngas can be burned in a burner to generate steam, which may be used for power generation or industrial heating. It can also be used as a fuel in a dedicated gas engine.

Fluidized bed reactors are used for solid to gas conversion processes thanks to their ability to furnish a high degree of gas-solid contact, fast solid-solid mixing, and fast gas mixing inside of the bed-zone owing to solids-induced flow. Further, fluidized bed biomass gasification is a promising technology for biomass gasification due to its compatibility with the physical and chemical properties of biomass, such as the high grinding cost and low energy density, which makes the adoption of entrained-flow gasification technology techno-economically impractical, as mentioned in [15].

Modeling of the gasification process pertains to the progress of volatile gasification homogeneous chemistry occurring in the gas phase and char particle combustion occurring in the Solid Phase as heterogeneous reactions. Thermodynamic equilibrium(i), kinetic (ii), and artificial neural network routes (iii) are the basic approaches for mathematical modeling of the gasification process as in [14]. Equilibrium or kinetic models, or a

combination of both have their advantages and disadvantages. Whereas equilibrium models are more straightforward in the formulation but do not yield satisfactory results for intricate reactor designs, the kinetic models are complicated in a formulation. Still, their predictions are more accurate compared to equilibrium models for sophisticated reactor designs. Various, Computational Fluid Dynamics (CFD) fulfills as a tool to examine the behavior of a given gasifier design by combining the advantages of both models [14]. Therefore, in this study, the gasification process inside Fluidized Bed Gasifier is modeled by CFD. A systematic description of the gasification processes inside the fluidized bed gasifier and temperature rises of both coal and air are given in Figure 4.

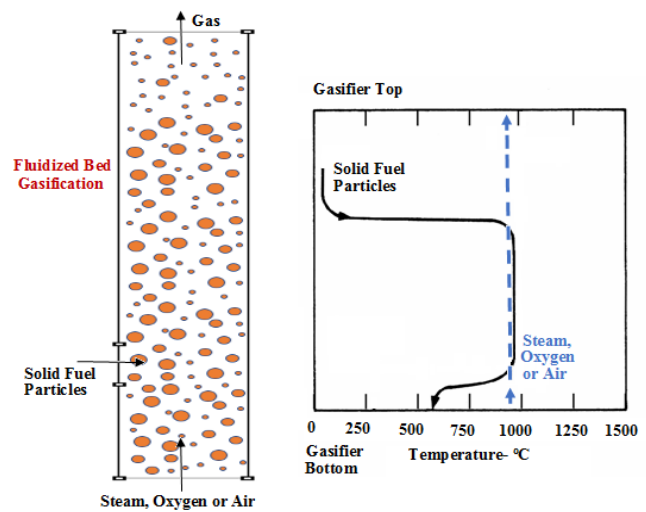


Figure 4. Fluidized bed gasifier [13].

As shown in Figure 4, this 2-D geometry is considered to simulate the gasification of solid waste particles, demonstrating the case set up for Eulerian-granular flow with the heterogeneous and homogeneous reactions. The gas and solid waste particles simultaneously enter the domain from different inlet sides of the geometry. In this case, both primary and secondary phases are modeled, considering as mixture. The primary phase is a gaseous mixture consisting of O_2 , N_2 , CO , CO_2 , tar, and H_2O . In contrast, the secondary phase is a solid waste mixture of $C(s)$, volatiles, $H_2O(l)$, and ash-coal, and initially contains 2% char and 2% volatiles. In this simulation, there are only two heterogeneous and one homogeneous reactions considered. Heterogeneous reactions are for devolatilization and char combustion reaction, whereas the homogeneous reaction is carbon monoxide converting to carbon-di-oxide [13]. The flowchart of the developed CFD model is shown in Figure 5.

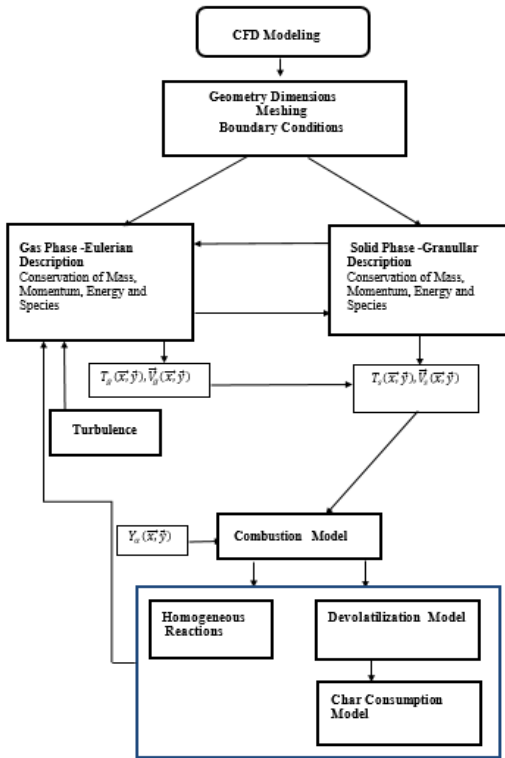


Figure 5. The flowchart of the developed CFD model.

2.1. Computational Domain and Boundary Conditions

Figure 4 is investigated by developing a 2-D planar CFD model, as shown below in Figure 6. Boundary conditions are chosen as velocity inlets (A: Inlet Solid Particules $V=0.2$ m/s, $T=300$ K and B: Inlet Gas $V=3$ m/s, and $T=1200$ K). Pressure outlet is chosen as Outlet Boundary (C: Outlet Gauge Pressure = 0 Pa), as shown in Figure 6. All other walls are considered as no-slip boundary conditions. They were modeled as an insulated wall. Heat conduction on gasifier walls was not taken into account. Convection and radiation heat transfer from gasifier walls to the environment were also neglected. The

the initial diameter of the solid particle was chosen as 0.0005m, the particle density value is 1400 kg/m³, the specific heat value of the particle is equal to 2092 J/kg K, and the thermal conductivity value of the particle is 1.5 W/mK.

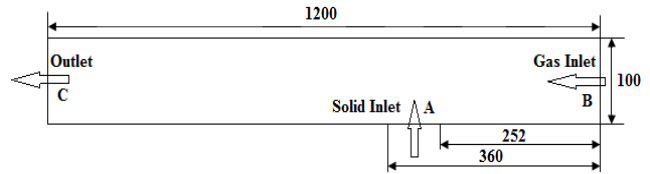


Figure 6. Geometry and dimensions (Dimensions are in mm).

2.2. Grid Independence Study and Mesh Structure

A grid independence study is required to obtain accurate results for all CFD analyses. Mesh is built by using triangular and prism cells of uniform grid spacing, as seen from Figure 7. Fine and uniform grid spacing was used for boundary layer meshes in the vicinity of the walls to effectively capture the hydrodynamics of fluidized bed reactors.

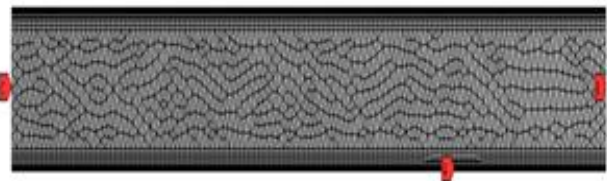


Figure 7. The grid structure of the CFD model.

Grid independency study is initially done by comparing various cell numbers with Maximum Phase 1 velocity changes, as seen below Figure 8; upon completion of this mesh independent study, 99424 elements are decided to be appropriate for accurate data resolution, as well as simulation time-consuming.

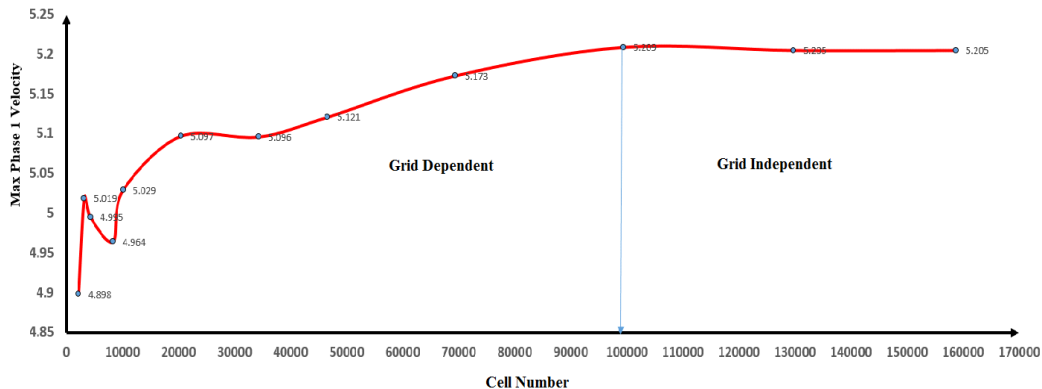


Figure 8. Maximum phase 1 velocity variation with cell number.

2.3. Turbulence Model

Turbulence modeling methods today can be grouped into the following three categories: Reynolds-Averaged Navier-Stokes (RANS) equations, Large Eddy Simulation (LES), and Direct Numerical Simulation (DNS) [16]. Although LES and DNS models are more accurate models than RANS ones, they were not used due to their high costly computing resources for industrial flow applications. RANS based standard k-ε turbulence model is generally used in the modeling of the turbulent flow for combustion and gasification processes in fluidized beds [17]. In this study, various RANS based turbulence models are investigated for determining the most suitable turbulence modeling to obtain reliable calculations of the dependent variable distribution, and several RANS based turbulence models are utilized in order to compare their consistency with the case. For the multiphase turbulence model, the dispersed option was chosen, and computations were performed by using ANSYS-FLUENT.

2.4. Multiphase Reactive Flow Modelling

The Eulerian-Granular modeling approach is used modeling multiphase reactive flow. This model is the most complex, accurate, and state-of-the-art computational technique to analyze multiphase flows in ANSYS FLUENT [18]. This model solves a set of conservation equations for mass species Eq. (1) and Eq. (4), for momentum transport, Eq. (2) and Eq. (5), and for energy transport Eq. (3) and Eq. (6). Those equations were solved for each primary and secondary phase along with the equation of granular temperature, developing the 2-D CFD model, as seen in Figure 9. Phases are coupled via the pressure and interphase exchange coefficients. This coupling approach is handled depends on the type of phases involved. The properties of Granular flow were obtained from the application of the kinetic theory.

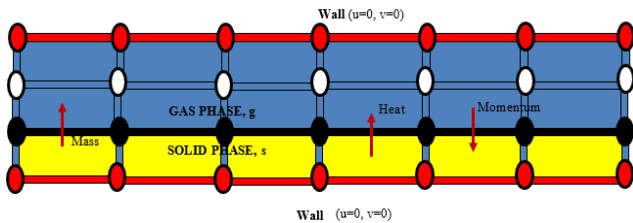


Figure 9. Scheme of CFD model, 2-D steady-state finite volume model.

-Gas Phase:

The species mass equation of gas phase;

$$\nabla \cdot (\alpha_g \rho_g Y_i \vec{v}_g) = \dot{m}_i + S_i \quad (1)$$

The momentum equation of gas phase;

$$\nabla \cdot (\alpha_g \rho_g \vec{v}_g \vec{v}_g) = -\alpha_g \nabla p + \nabla \cdot \bar{\tau}_g + \alpha_g \rho_g \vec{g} + K_{sg} (\vec{v}_s - \vec{v}_g) + \dot{m}_{sg} \vec{v}_{sg} \quad (2)$$

The energy equation of gas phase;

$$\nabla \cdot (\alpha_g \rho_g \vec{v}_g \vec{v}_g H_g) = \bar{\tau}_g : \nabla \vec{v}_g + \nabla \cdot \vec{q}_g + S_g + Q_{sg} + \dot{m}_{sg} H_{sg} \quad (3)$$

-Solid Phase:

The species mass equation of solid phase;

$$\nabla \cdot (\alpha_s \rho_s Y_i \vec{v}_s) = \dot{m}_i + S_i \quad (4)$$

The momentum equation of the solid phase;

$$\nabla \cdot (\alpha_s \rho_s \vec{v}_s \vec{v}_s) = -\nabla p_s + \nabla \cdot \bar{\tau}_s + \alpha_s \rho_s \vec{g} + \dot{m}_{sg} \vec{v}_{sg} \quad (5)$$

The energy equation of the solid phase;

$$\nabla \cdot (\alpha_s \rho_s \vec{v}_s H_s) = \bar{\tau}_s : \nabla \vec{v}_s + \nabla \cdot \vec{q}_s + S_s + Q_{sg} + \dot{m}_{sg} H_{sg} \quad (6)$$

Mass, momentum, and energy Interphase exchange between these phases is dependent upon the type of mixture being modeled, as shown in Figure 10, mass, momentum, and heat transport at the interface. Interface transport equations, Eq. (7), Eq. (8), Eq. (9) were solved:

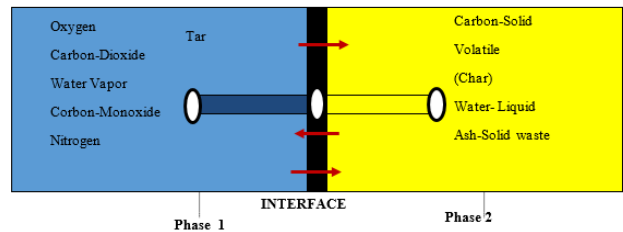


Figure 10. Material mixtures, mixture gas (phase 1) & mixture solid (phase 2).

$$m_p C_p \frac{dT_p}{dt} = h A_p (T_\infty - T_p) + \frac{dm_p}{dt} h_{sg} + S_x \quad (7)$$

$$-Q_{sg} = Q_{sg} = \frac{6K_g \alpha_s \alpha_g Nu_s}{L_s^2} (T_s - T_g) \quad (8)$$

Nusselt number is correlated by Gunn [19];

$$Nu_s = (7 - 10\alpha_g + 10\alpha_g^2)(1 + 0.7Re_s^{0.2} Pr_g^{0.33}) + (1.33 - 2.4\alpha_g + 1.2\alpha_g^2) Re_s^{0.7} Pr_g^{0.33} \quad (9)$$

2.5. Modelling Chemical Reactions and Species Modelling

Chemical reactions are modeled by using a volumetric reaction in Species Transport, while the Finite-Rate/Eddy Dissipation Model is used for Turbulence and Chemistry Interaction. Species transport Eq. (10) is solved, and the convection-diffusion equation is used to compute the mass fraction of each specie Y;

$$\frac{\partial(\rho Y_j)}{\partial t} + \nabla \cdot (\rho Y_j V) = -\nabla \cdot J_j + R_j + S_j \quad (10)$$

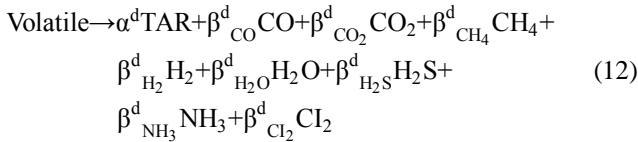
For the realistic coal combustion or gasification process, it is necessary to consider more heterogeneous and homogeneous reactions. Two heterogeneous reactions are considered, one for char combustion and the other for devolatilization, and three reactions are only used for this study.

Chemical reactions of the gasification process are as follows;

a-) Char Combustion, Heterogenous Reaction, as formulated in Eq. (11);



b-) Devolatilization, Heterogeneous Reaction, as shown in Eq. (12);



c-) CO combustion, homogeneous reaction;



Along with more reactions, the efficiency of the gasification process would be higher, and much more accurate, as well as gasification process simulation, would be much closer to real gasification. Gasification process should also be optimized by means of the size of the feeding material particles, the shape of the particles, the structure of the material (porous, non-porous), environment (reactive Air/Oxygen, Inert Nitrogen/Argon), flow of the medium, heating rate (slow-fast), Temperature (Low <500°C, High >500°C).

Radiation calculation should also be considered to get a more accurate temperature distribution on the gasifier domain. This work only demonstrates the use of multiphase flow along with chemical reactions, without considering radiation.

2.6. Model Validation

This CFD model is validated by Liu’s work [20], as seen in Figure 11, and Solid Volume Fraction was compared, as shown in Figure 12 and Figure 13. The agreement between the present numerical results and Lui’s results is quite similar. For model validation, another asymmetric model was prepared exactly the same as Lui’s study, including the same 2-D dimensions with similar boundary conditions in order to compare both models’ results. Lui’s findings, which is time-averaged solid volume fraction, were compared with solid volume fraction distribution of this present study. As shown in Figure 13, a point value comparison was fulfilled. The maximum solid volume fraction was 0.565; on the other hand, Lui’s maximum solid volume fraction value was 0,559. Error percentage was also very low as % 1.07 when comparing both models.

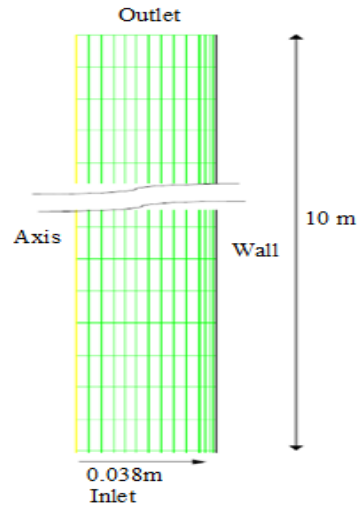


Figure 11. Geometry dimensions, mesh structure, and boundary conditions of the Hui Liu Model [20].

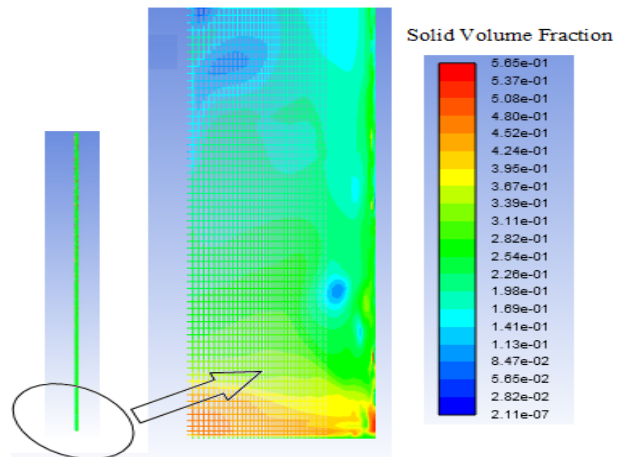


Figure 12. Solid volume fraction distribution contour results of the present study.

2.7. Numerical Procedure

The gasification process is analyzed by using commercial software ANSYS-FLUENT, which is a finite volume method based CFD pressure solver. Pressure based solver was used. The gravity force was taken into account. Moreover, viscous heating was neglected for this calculation. The phase-couple SIMPLE scheme is used for solving the pressure-velocity coupling. The cell center method was used. The mesh was generated by using triangle cells with uniform grid spacing. The second-order upwind scheme was used to discretize the convective terms in the momentum, mass, and energy equations. The gas-solid multiphase flow was previously solved without using energy equations and chemical reactions to find a stable solution. The chemical reactions and heat transfer modes were included, and the full reactive flow system was solved after finding a sufficient flow pattern. The convergence criterion was $10e-6$ for residuals of the continuity and momentum equations and $10e-10$ for residual energy equation. $k-\epsilon$ Standart turbulence model and standard wall function were used for calculations.

3. Results and Discussion

After the full non-linear coupled partial differential equations are solved by this developed CFD model, results were visualized by colorful contours, initially as seen in Figure 13, which shows a molar concentration of CO distribution in the domain. Carbon monoxide is the main product of the gasification process. Therefore, it is initially critical to analyze the amount of CO. It also shows efficient gasification locations.

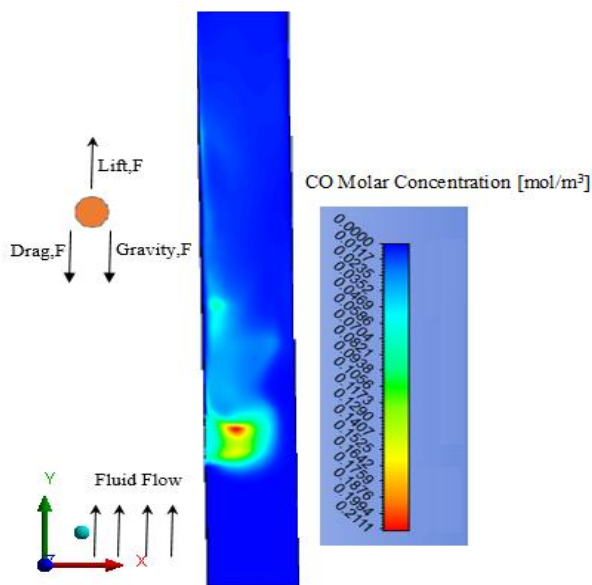


Figure 13. The molar concentration of CO for phase 1.

Numerous parameters can be calculated by this developed CFD model, like dynamic viscosity, species concentration, pressure, velocity, and temperature distributions of this mixture flow, and they can be investigated, which are the important reactive flow properties. For instance, velocity distribution can be analyzed for both phase 1 and phase 2, as seen in Figure 14. Particle pathlines and gas streamlines were prepared together in Figure 14. It does show particle behaviors in the hot gas flow, and it is critical to visualize both particle pathlines and gas streamlines in terms of proper gas-solid mixing and more efficient gasification or combustion.

Figure 15 shows the turbulence kinetic energy and velocity relations. Turbulence kinetic energy is higher where the chemical reactions have occurred, and phase velocities are getting higher when to combine phase 1 and phase 2. Turbulence kinetic energy indicates turbulence intensity occurring in the flow, and it can visualize higher turbulence locations in the flow domain. Velocity distribution is also critical for design gasifier. Min velocity values close to zero shows dead areas in the flow domain, and Max velocity values show, especially particle higher velocities, can cause damage on gasifier walls. By the way, homogenous distribution velocity means homogenous gas and solid mixing. Proper mixing does increase the efficiency of gasification or combustion processes. When turbulence kinetic energy increases, gasification efficiency would increase, and the right mixing conditions would have occurred.

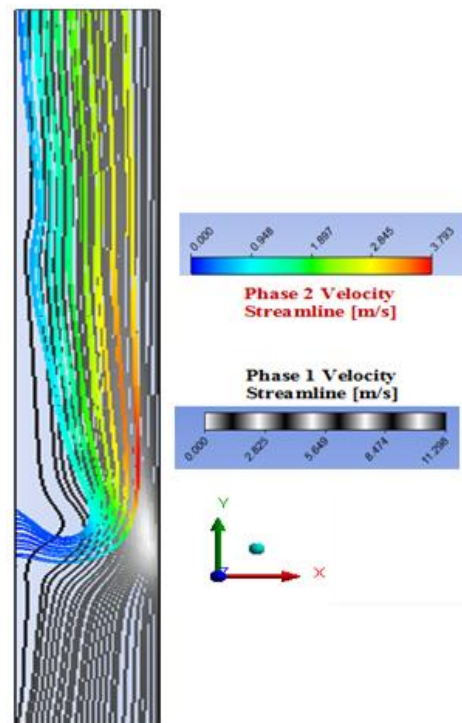


Figure 14. Phase 1 and phase 2, velocity streamlines.

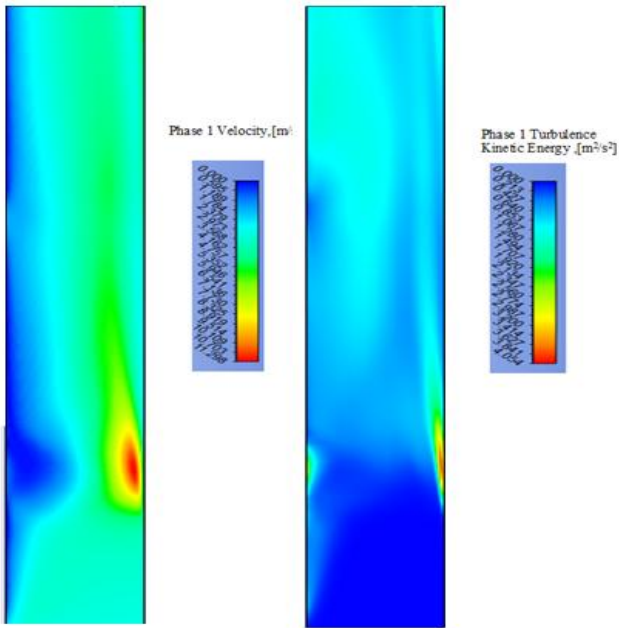


Figure 15. Phase 1 Turbulence kinetic energy and velocity distribution.

Calculations of energy efficiency and gasification performance were calculated following Eq. (15) and Eq. (17) by using Eq. (14) and Eq. (16).

Cold gas efficiency;

$$\eta_m = \frac{H_g Q_g}{H_s M_s} \times 100 \quad (14)$$

$$\eta_m = \frac{15000 \frac{\text{kJ}}{\text{m}^3} \times 3.385786 \text{ m}^3/\text{sn}}{13400 \frac{\text{kJ}}{\text{kg}} \times 6.4067 \text{ kg}/\text{sn}} \times 100 \Rightarrow \eta_m = \% 59 \quad (15)$$

Hot gas efficiency;

$$\eta_m = \left(\frac{H_g Q_g + Q_g \rho C_p (t_g - t_a)}{H_s M_s} \right) \times 100 \quad (16)$$

where $H_{\text{sensible}} = C_p Q_g \rho (t_g - t_a)$

$$\eta_m = \frac{15000 \times 3.385786 + 6200 \text{ kJ}/\text{sn}}{13400 \frac{\text{kJ}}{\text{kg}} \times 6.4067 \text{ kg}/\text{sn}} \times 100 \Rightarrow \eta_m = \% 66 \quad (17)$$

Gasification efficiency is an important factor in determining parameters of constructing a gasifier in terms of economic feasibility. For thermal applications, if synthetic gas is not cooled before the combustion process, the efficiency of gasification is formulated as the addition of sensible heat of the gas, as shown in the above correlations.

Cold gas efficiency as 59% and hot gas efficiency as 66% obtained were normalized values, comparing to the highest efficiency. The gasifier efficiency would be

increased more with the process and design parameters optimization.

This work can be compared with Couto et al.'s study [21], as seen in the following results in Figure 16, although Couto et al.'s research and this present study are modeled with different domain size and using different boundary conditions [21]. Contours of CO₂ mole fractions were compared. Carbon monoxide is also a combustible product of the gasification process. It is good to calculate the amount of CO₂ and visualize CO₂ distribution in the flow domain.

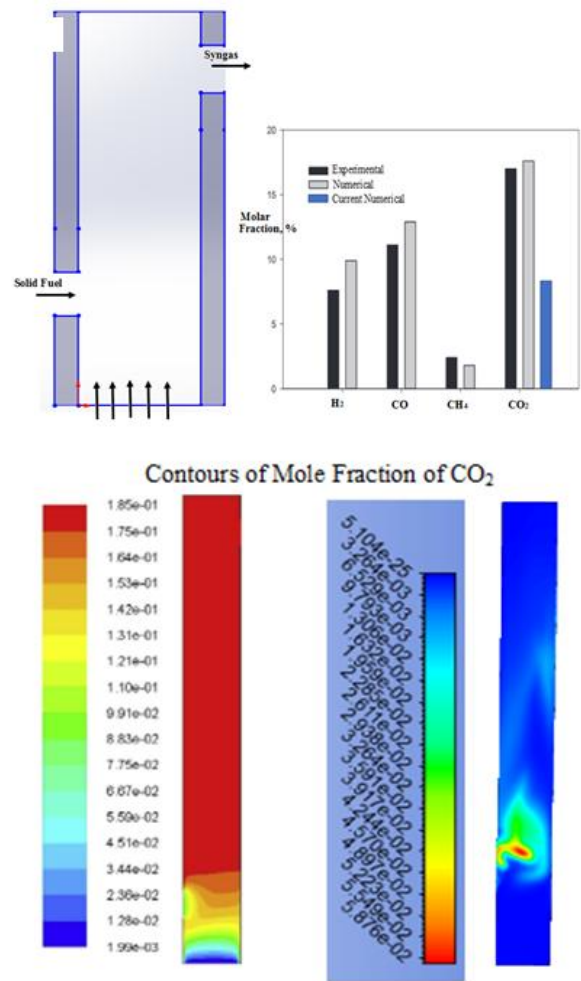


Figure 16. Mole fraction comparison of present results with experimental and numerical results of Couto et al. [21].

In addition to those above findings and explanations, gasification performance is evaluated in terms of the particle size diameter. For some calculations, syngas efficiency is increased when the diameter of the solid particle is decreased. For instance, when the particle diameter was 0.00050 m, syngas flow rate 0.121 kg/s when the diameter was reduced to 0.00001 m, the syngas flow rate was getting an increase to 0.0125 kg/sn.

Solid particle diameter was tried to optimize as one of the essential process parameters. For the gasifier design, turbulence modeling was carefully researched for gasification performance and syngas quality. As shown below, Tables (1-4) results of RANS based commonly used turbulence models are initially compared with each other for various wall functions. A double mesh structure was used to compare turbulence models. Mesh structure was changed to make y plus value around 1.5 when to use all enhanced wall treatments. Y plus value was around 4 for all other wall functions.

Reynolds stress turbulence model with enhanced wall treatment, as seen in Table 1, has correctly calculated Solid Volume Fraction and phase1 velocity. On the other hand, the Reynolds stress model with standard wall function has calculated the solid volume fraction very accurately (0.5959424); however, phase 1 velocity value was not accurate (18.85557m/s) as much as generated previously with enhanced wall treatment. The cell height next to the wall should be coarsened when using this standard wall function. Y plus value should be increased to at least around 30 to get more accurate results for standard wall functions. Overall, Reynolds stress turbulence models are time-consuming and hard to stabilize the numerical scheme when comparing k-ε models.

k-ω Standard, SST, and BSL models were compared, as shown in Table 2. k-w models do not need wall function treatment since they need y+ to be 1. Y plus value was the maximum point value equals 1.5. Results were in acceptable ranges; however, solid volume fraction and phase 1 velocity calculated by those models were little far away from the accurate results. On the other hand, numerical stability and time-consuming factors are satisfactory, comparing to Reynolds stress models.

Table 1. Reynolds stress turbulence model comparison.

RANS based Turbulence Models	Wall Function	Solid Volume Fraction	Phase1 Velocity
Reynolds Stress (5 equation)	Enhanced Wall Treatment	0.629496	11.24822 m/s
Reynolds Stress (5 equations)	Standard Wall Function	0.5959524	18.85557 m/s

RANS are completely different than RSM (Reynolds Stress Models). So it is seen that the results also compared RANS with RSMs. RANS (Reynolds Average Navier

Stokes Equations) based turbulence models were compared, as seen Tables (1-4).

Table 2. k-ω turbulence model comparison.

RANS based Turbulence Models	Wall Function	Solid Volume Fraction	Phase 1 Velocity
k-ω Model SST	-	0.629496	10.54487 m/s
k-ω Model BSL	-	0.5620949	12.12203 m/s
k-ω Model Standart	-	0.629496	12.99466m/s

Table 3. k-ε standard turbulence models.

RANS based Turbulence Models	Wall Function	Solid Volume Fraction	Phase 1 Velocity
k-ε Model Standard	Menter-Lechner	0.629496	14.50941 m/s
k-ε model Standard	Enhanced Wall Treatment	0.629496	19.85524 m/s
k-ε model Standard	Non-equilibrium Wall Function	0.629496	8.876338 m/s
k-ε model Standard	Scalable Wall Function	0.629496	9.869212 m/s
k-ε model Standard	Standard Wall Function	0.615978	10.77692 m/s

Results are more efficient with k-ε turbulence models when to use standard wall function, and Reynolds stress five equations model with enhanced wall treatment. Standart wall function, which is a near-wall treatment approach, is used when y+ value is greater than 30. When y+ value is equal to 1, two equations k-ε turbulence model with enhanced wall treatment generates more accurate results than others. In addition to the above conclusion, when choosing a reliable turbulence model, higher convergence residual, numerical stability, and fast solving

issues were considered as well. Y plus values were used as 1.5 and 4 for current work, which was the maximum point values of the computational domain.

Table 4. k- ϵ RNG turbulence model.

RANS based Turbulence Models	Wall Function	Solid Volume Fraction	Phase 1 Velocity
k- ϵ Model RNG	Menter-Lechner	0.629496	10.62368m/s
k- ϵ model RNG	Enhanced Wall Treatment	0.629496	11.66239 m/s
k- ϵ model RNG	Non-equilibrium Wall Function	0.629496	8.876338 m/s
k- ϵ model RNG	Scalable Wall Function	0.629496	9.93663m/s
k- ϵ model RNG	Standard Wall Function	0.615978	10.77692 m/s

4. Conclusion

In this 2-D study, the complex gasification process inside fluidized bed gasifier by considering two heterogeneous and one homogeneous reaction were modeled by developing a CFD model.

The standard k- ϵ model with standard wall function was used in this study since RANS based standard k- ϵ turbulence model is generally used in the modeling of the turbulent flow for combustion and gasification processes in fluidized beds. The performance of this model was also compared with RSM (Reynolds Stress Model) model and RNG k- ϵ model with various wall functions to check the suitability of the model. Results were satisfactory by using the Reynolds Stress model with enhanced wall treatment, as mentioned, and highlighted the text with a blue color in Table 1. k- ϵ model with standard wall function has generated the best proper results among the above turbulence models, as mentioned in Table 3, even if y plus value was around 4. k- ϵ RNG turbulence model has also generated very similar results with the k- ϵ model with standard wall function.

Two heterogeneous reactions are considered, one for char combustion and the other for devolatilization, and three reactions are used for this study.

After the full non-linear coupled partial differential equations are solved by developed CFD model, molar concentration of CO, phase 1 and phase 2 velocity streamlines, phase 1 Turbulence kinetic energy and velocity distribution, and contours of mole fraction of CO₂ were obtained.

Gasification efficiency is an important factor in determining parameters of constructing a gasifier in terms of economic feasibility. Cold gas efficiency and hot gas efficiency were calculated as 59% and 66%.

This developed CFD model would have a significant impact on gasifier design, process optimization, and it would also be used as a research tool.

Acknowledgment

This research is sponsored by the Department of Mechanical Engineering at Bursa Uludag University, Council of Higher Education (YOK) with grand number 100-2000, and TUBITAK with 2211 Project Award.

References

- [1] Levendis A. Y., Atal A., Carlson B. J., Quintana M. M. E., 2001. PAH and Soot Emissions from Burning Components of Medical Waste: Examination/Surgical Gloves and Cotton Pads. *Chemosphere*, **42**(5-7), pp. 775-783.
- [2] Monteiro E., Couto N., 2015. Numerical and Experimental Analysis of Municipal Solid Wastes Gasification Process. *Applied Thermal Engineering*, **78**, pp. 185-195.
- [3] Mellin P., Kantarelis E., Zhou C., Yang W., 2014. Simulation of Bed Dynamics and Primary Products from Fast Pyrolysis of Biomass: Steam Compared to Nitrogen as A Fluidizing Agent. *Industrial Engineering Chemistry Research*, **53**, pp. 12129-12142.
- [4] Gunarathne S. D., Mueller A., Fleck S., Kolb T., Chmielewski J. K., Yang W., Blasiak W., 2014. Gasification Characteristics of Steam Exploded Biomass in An Updraft Pilot Scale Gasifie. *Energy*, **71**, pp. 496-506.
- [5] Horton R. S., Zhang Y., Bennett A. C., Klein T. M., Petrocelli F., 2016. Molecular-Level Kinetic Modeling of Biomass Gasification. *Energy&Fuels* **30**, pp. 1647-1661.

- [6] Pour S. M., Weihong Y., 2014. Performance of Pulverized Coal Combustion under High Temperature Air Diluted by Steam. *ISRN Mechanical Engineering*, **2014**, pp. 217-227.
- [7] Zhou C., Stuermer T., Gunarathne R., Yang W., Blasiak W., 2014. Effect of Calcium Oxide on High-Temperature Steam Gasification of Municipal Solid Waste. *Fuel*, **122**, pp. 36-36.
- [8] Li J., Bonvicini G., Tognotti L., Yang W., Blasiak W., 2014. High-Temperature Rapid Devolatilization of Biomasses with Varying Degree of Torrefaction. *Fuel*, **122**, pp. 261-269.
- [9] Kantarelis E., Yang W., Blasiak W., 2014. Effect of Zeolite to Binder Ratio on Product Yields and Composition During Catalytic Steam Pyrolysis of Biomass over Transition Metal Modified. *Fuel*, **122**, pp. 119-125.
- [10] Mellin P., Kantarelis E., Yang W., 2014. Computational Fluid Dynamics Modeling of Biomass Fast Pyrolysis in A Fluidized Bed Reactor, Using A Comprehensive Chemistry Scheme. *Fuel*, **117**, pp. 704-715.
- [11] Gunarathne S. D., Chmielewski K. J., Yang W., 2014. Pressure Drop Prediction of A Gasifier Bed with Cylindrical Biomass Pellets. *Applied Energy*, **113**, pp. 258-266.
- [12] Schulze S. A., Richter M., Vascellari A., Gupta B., Meyer P., Nikrityuk A., 2016. Novel Intrinsic-based Sub Model for Char Particle Gasification in Entrained-flow Gasifiers: Model Development, Validation and Illustration. *Applied Energy*, **164**, pp. 805-814.
- [13] ANSYS Inc., 2016. Modeling Heterogeneous Reactions with Eulerian-Granular Flow, pp. 16-25.
- [14] Baruah D., Baruah D. C., 2014. Modeling of Biomass Gasification: A Review. *Renewable and Sustainable Energy Reviews*, **39**, pp. 806-815.
- [15] Addison K. S., Altantzis C., Bates R. B., Ghoniem A. F., 2016. Towards An Advanced Reactor Network Modeling Framework for Fluidized Bed Biomass Gasification: Incorporating Information from Detailed CFD Simulations, *Chemical Engineering Journal*, **303**, pp. 409-424.
- [16] Versteeg H. K., Malalasekera W., 2007. *An Introduction to Computational Fluid Dynamics*, 2nd ed., Pearson Education Limited, Harlow, England.
- [17] Bakul C. E. J., Gershtein V. Y., Xianming L., 2001. *Computational Fluid Dynamics in Industrial Combustion*, 2nd ed., NY CRC Press, New York, US.
- [18] FLUENT Inc., 2001. *Introduction to Modelling Multiphase Flow*, 18-12.
- [19] Gunn D. J., 1978. Transfer of Heat or Mass to Particles in Fixed and Fluidized Beds. *International Journal of Heat and Mass Transfer*, **21**, pp. 467-476.
- [20] Liu H., 2014. *CFD Modeling of Biomass Gasification Using A Circulating Fluidized Bed Reactor*, Ph.D. Thesis, Waterloo University, Ontario, Canada.
- [21] Couto N., Silva V., Monteiro E., Paulo Brito P., Rouboa A., 2015. Using An Eulerian-granular 2-D multiphase CFD Model to Simulate Oxygen Air Enriched Gasification of Agroindustrial Residues. *Renewable Energy*, **77**, pp. 174-181.



Non-equilibrium Molecular Dynamics for Calculating the Thermal Conductivity of Graphene-Coated Aluminum

Kasim TOPRAK ^{1,*} , Ahmet Berk YILMAZ ² 

¹ Department of Mechanical Engineering, Izmir Institute of Technology, Izmir, 35430, Turkey, **ORCID:** 0000-0002-0043-2941

² Department of Energy Engineering, Izmir Institute of Technology, Izmir, 35430, Turkey, **ORCID:** 0000-0003-4601-9068

Abstract

Article Info

Research paper

Received : December 23, 2019

Accepted : August 11, 2020

Keywords

Graphene-coated Aluminum
Molecular Dynamics
Size Effect
Thermal Conductivity

Non-equilibrium Molecular Dynamics (NEMD) simulations have been created in C++ using Message Passing Interface (MPI) library to calculate the phonon thermal conductivity of bare graphene, aluminum, and graphene-coated aluminum. This study focuses on how graphene can alter the thermal conductivity of graphene-coated aluminum. The effect of length, graphene, and the number of graphene layers are analyzed. Even though electrons are dominant on thermal conductivity of aluminum, the effect of graphene coating can be seen in the results. The results show that the thermal conductivity of aluminum increases by up to 149% by graphene coating. When the number of layers increases to two layers, the thermal conductivity increases by up to 261%. Moreover, the results increase with the length of all models.

1. Introduction

The development in computer and materials sciences enable us to create new devices in many areas including automotive and aerospace. At the same time, these new devices must work under heavily loaded operations. These operations generate heat as a by the production of operation. Among metals, aluminum has been adopted in these devices owing to its high thermal conductivity value among metals. However, higher thermal conductivity materials are needed for these advanced applications to keep them under the required working conditions [1]. In the literature, there have been various materials including Carbon Nanotubes (CNTs), diamond, graphite, and graphene used to obtain the need for thermal management.

Graphene is one of the materials that has the highest thermal conductivity value among carbon allotropes. It also has lightweight, high mechanical, and electrical properties [2–5]. These properties make graphene attractive material among thermal applications [6].

Researchers have been working on graphene to use in many areas. It has been used as pure graphene and reinforcing or coating material to enhance material properties.

Many attempts have been done for producing graphene reinforced Aluminum Metal Matrix Composites (AMMCs). For instance, graphene reinforced AMMCs are produced with Friction Stir Processing (FSP) [7], powder synthesis [8–10], vacuum hot pressing [11], and Chemical Vapor Decomposition (CVD) methods [12]. Jeon et al. [7] studied graphene reinforced AMMC fabrication by FSP and the results showed that the thermal conductivity was 15% higher than the bare aluminum. Another research showed that a 15.4% enhancement in thermal conductivity can be achieved by adding graphene into pure Al by powder metallurgy technique [13]. Zheng et al. [12] synthesized graphene-coated aluminum alloy by transferring the CVD grown graphene on aluminum alloy. Aluminum alloy's anti-corrosion property enhanced via graphene coating. The corrosion resistance of aluminum studies has been done by other researchers in the literature and it was also found that the graphene layer protects the aluminum against corrosion [14]. Moreover, Han et al. [15] were fabricated nanotube@Cu/Ag@graphite/Al composite.

* Corresponding Author: kasimtoprak@iyte.edu.tr

This article is an extended version of the paper presented at the 22nd Congress on Thermal Science and Technology.



The results showed that 0.1 mm graphite enables composite to have 48.8% higher thermal conductivity, stable coefficient of thermal expansion at a high temperature, and 126% higher bending strength compared to without graphite film. Abhinav et al. [16] made up of an aluminum box and a graphene-coated aluminum box to compare heat transfer and electrical resistance. The results showed that the temperature of the inside graphene-coated aluminum box is 36% higher than the uncoated one. The electrical resistance value was also decreased by 33%.

The studies on graphene are not limited to experimental ones; the numerical calculation has been done in the literature. One of the most widespread methods of Molecular Dynamics (MD) is an atomistic simulation technique to study the properties of nano-sized materials. Zhang et al. [17] studied the length effect on the thermal conductivity of supported graphene and achieved that TC increases with the length. Cao [18] studied MD simulation to show the temperature effect of graphene on the TC. The

results showed that the TC decreases from $1600 \text{ Wm}^{-1}\text{K}^{-1}$ to $400 \text{ Wm}^{-1}\text{K}^{-1}$ as the temperature increases from 300 K to 1000 K. In addition to pure graphene, the mechanical behavior of graphene-coated aluminum is investigated. The Young modulus of aluminum increases with graphene coating by 88% [19].

NEMD simulation code is created in the C++ programming language using Message Passing Interface (MPI) library and the code is used to investigate the length dependence and graphene coating effect on the phonon thermal conductivity (κ_{ph}) of aluminum.

2. Method

A zig-zag structure graphene-coated aluminum that has a Face-centered Cubic (FCC) structure with a lattice constant of 4.04 \AA models is created. Figure 1 illustrates the schematic model of graphene-coated aluminum with calculation zones.

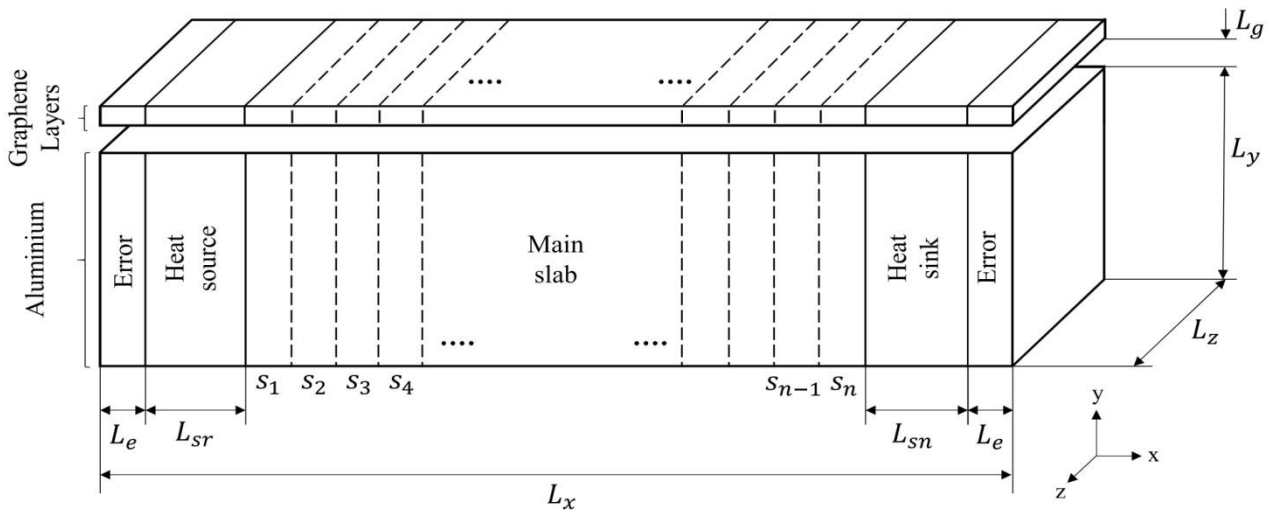


Figure 1. Schematic illustration of the simulation domain.

The height (L_y) and width (L_z) of the aluminum block are kept at 16 \AA during the simulations. The simulation models have three calculation zones; error, thermostat, and main. Two error zones are created and placed at each end of the modeled materials. Their lengths (L_e) are kept at 3 \AA . The thermostat zones have placed both edges between the main zone and error zones and kept at 320 K as a heat source and 280 K as a heat sink using the Nose-Hoover thermostat. Nose Hoover thermostat is one of the numerical methods used to control the temperature by maintaining the velocities [20]. The relaxation time of the thermostats, τ , is selected as 50 fs . The length of the heat source (L_{sr}) and sink (L_{sn}) are 8 \AA . The main zone or main slab is where the length effect is investigated. The main slab is virtually sliced into 8 sections. The length of each section is equal to each other.

The lengths of the modeled materials (L_x) are $60, 100, 200,$ and 250 \AA to predict the length effect on the phonon thermal conductivity (κ_{ph}). The length between the top of the aluminum block and the graphene layer (L_g) is 3 \AA [21]. The length between each graphene layer is 3.4 \AA for multiple layers graphene [22].

The C-C bonding interactions in graphene layers are calculated by the Tersoff potential;

$$U_{TE}(r_{ij}, r_{ik}, \Theta_{ijk}) = f_{ij}^{Ct} \left[a_{ij} A e^{-\lambda_1 r_{ij}} - b_{ij} B e^{-\lambda_2 r_{ij}} \right] \quad (1)$$

where C is the cut-off function and b_{ij} is the bond angle terms. The rest of Tersoff potential parameters are $A=1393,6 \text{ eV}$, $B=346,74 \text{ eV}$, $\lambda_1=3.4879 \text{ \AA}$, $\lambda_2=2.2119 \text{ \AA}$, $n=0.72751$, $c=38049$, $d=4.3484$, $h=-0.57058$,

$\beta=1.5724*10^{-7}$, $R_{ij}=1.8 \text{ \AA}$, $S_{ij}=2.1 \text{ \AA}$, and $a_{ij}=1$ [23]. The Al-Al interactions are described as the Sutton-Chen potential which is on the Embedded Atom Method (EAM) potential;

$$U_{SC}(r_{ij}) = \left[\sum_{j \neq i}^N \epsilon \frac{1}{2} \left(\frac{\sigma}{r_{ij}} \right)^n - c \sqrt{\sum_{j \neq i}^N \left(\frac{\sigma}{r_{ij}} \right)^m} \right] \quad (2)$$

where $\epsilon_{Al-Al} = 0.033147 \text{ eV}$, $m=6$, $n=7$, $c=16,399$ [24]. The nonbonding interactions between the aluminum block and graphene layer which is Al-C and between each graphene layer which is C-C are assumed as the Lennard-Jones potential;

$$U_{LJ}(r_{ij}) = 4\epsilon \left[\left(\frac{\sigma}{r_{ij}} \right)^{12} - \left(\frac{\sigma}{r_{ij}} \right)^6 \right] \quad (3)$$

where $\epsilon_{Al-C} = 0.035078 \text{ eV}$ and $\sigma_{Al-C} = 3.0135 \text{ \AA}$ for Al-C interactions [21] and $\epsilon_{C-C} = 0.002168 \text{ eV}$ and $\sigma_{C-C} = 3.36 \text{ \AA}$ for C-C interactions [25]. The numerical integrations are calculated using the Velocity-Verlet integration algorithm with 0.5 fs timestep [26].

The molecular model of a single layer graphene-coated aluminum block is seen in Figure 2.

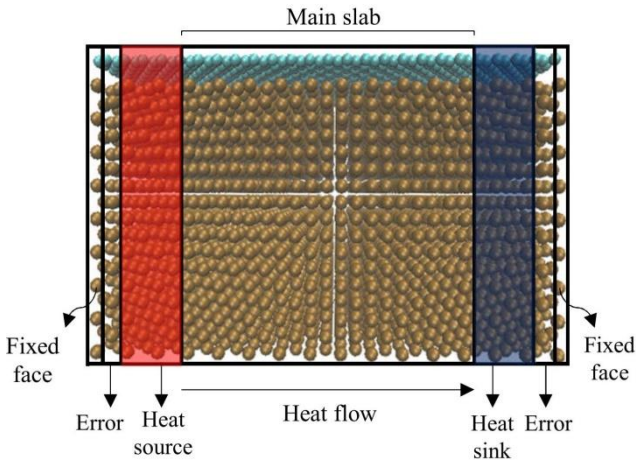


Figure 2. Single-layer graphene-coated aluminum.

A single atomic layer of aluminum is fixed at both the left and right ends of the models. The simulations are first to run 0.125 ns to equilibrate the system temperature at 300 K. Following the system reaches the temperature of 300 K, the heat source at 320 K and heat sink at 280 K are applied to the model for 14.875 ns. After the temperature differences, the simulations are continued for 5 ns where the thermal conductivity is calculated. During the last period, the temperature gradients and thermostat energy change data are collected. Using the Fourier law approach and the simulation data, the thermal conductivity is

calculated as follows [27];

$$\kappa_{ph} = \frac{\Delta E_{avg}}{A \Delta t \frac{\Delta T}{\Delta x}} \quad (4)$$

where Δt is the simulation time, $\Delta T/\Delta x$ is the temperature gradient of the main slab, A is the cross-sectional area, and ΔE_{avg} is the average energy changes in the heat source and sink. It is the mean energy that is added and subtracted in thermostat regions. It is calculated from the energy differences between before and after thermostats applied to both heat source and heat sink parts.

3. Results

The phonon thermal conductivity of pure graphene, uncoated aluminum, and graphene-coated aluminum was predicted. For comparison, the length effect on the thermal conductivity was calculated for each model. The length effect on the suspended graphene in the range from 60 to 250 \AA is calculated and shown together with the results by Wei et al. [22] in Figure 3. Single-layer graphene with a thickness of 3.4 \AA was used during pure graphene simulations. As seen in the results, the length dependence of bare graphene shows similar results and increases with length.

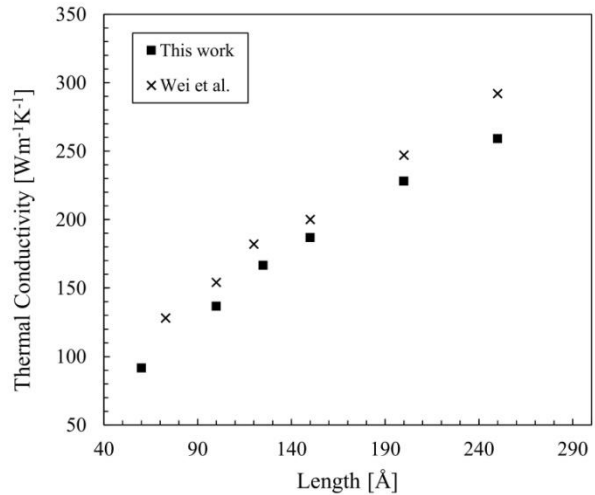


Figure 3. The phonon thermal conductivity of single layer graphene.

Even though heat transport is dominated by phonon in graphene, it is maintained by electrons in metals. Figure 4 shows the length effect on the phonon thermal conductivity of aluminum with a temperature gradient through a longitudinal direction. The results show that the thermal conductivity increases. The thermal conductivity of aluminum is 205 W/mK in the literature, however, the obtained results are much smaller since the MD simulation

results are phonon interactions. Still, the simulated results are similar to the literature [28-29].

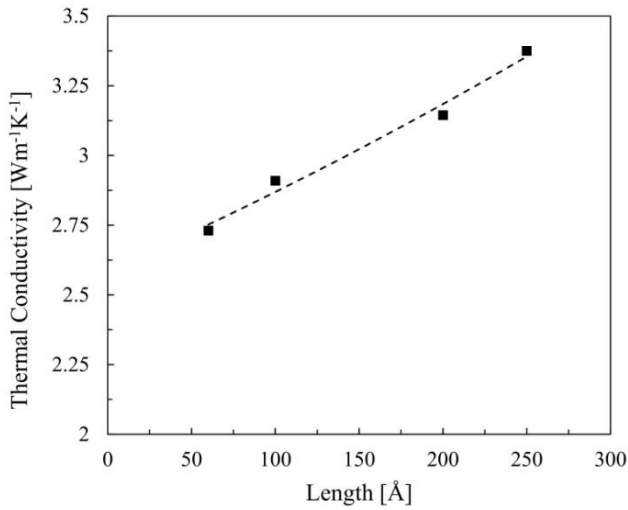


Figure 4. The length dependence of phonon thermal conductivity of aluminum.

After simulating and calculating the phonon thermal conductivity of graphene and aluminum individually, graphene-coated aluminum is modeled to investigate its results. Figure 5 shows the length and number of graphene coating layer effects on the thermal conductivity of graphene-coated aluminum.

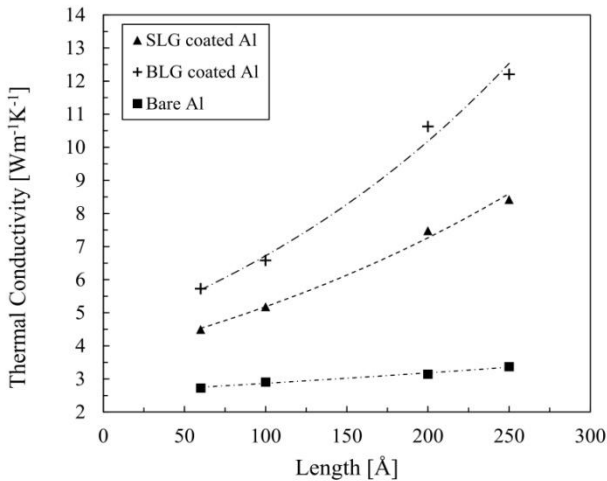


Figure 5. Phonon thermal conductivity of bare aluminum, SLG coated aluminum, and BLG coated aluminum.

As seen from the results, the thermal conductivity increases for all models with the length. There is also a significant increase in thermal conductivity with graphene coating. There is an up to 149% increase with Single-Layer Graphene (SLG) coated aluminum and up to 261% increase with two-layer graphene layers (BLG) coated aluminum. Accordingly, the C-Al interactions and the

unique properties of graphene help to increase heat transfer on the graphene-coated aluminum. This means that the thermal transport in graphene-coated aluminum is ballistic. Additionally, it is believed that increasing the number of graphene coating layers limits the phonon scattering and increases the phonon mean free path which results in increasing the thermal conductivity.

4. Conclusions

In the present study, a NEMD simulation code in C++ with MPI library was created to explore the phonon thermal conductivity of bare graphene, aluminum, and graphene-coated aluminum. Thermal conductivity of graphene-coated aluminum increases with a length which is seen similar results in bare graphene and aluminum. Due to the interaction of C-Al and C-C, the thermal conductivity of graphene coating on aluminum increases the thermal conductivity. Increasing the number of coating graphene layers shows an enhancement in the thermal conductivity for bare aluminum. Even though electrons dominate on the thermal conductivity of aluminum, the graphene coating on aluminum shows a distinctive contribution to the phonon thermal conductivity. By the results of this study, graphene coating may enable aluminum to be used in need of high thermal management.

Acknowledgements

The numerical calculations reported in this paper were partially performed at TUBITAK ULAKBIM, High Performance and Grid Computing Center (TRUBA Resources). This work was supported by the Scientific and Technological Research Council of Turkey (TUBITAK), Project No: 116F115.

References

- [1] Balandin A. A., 2009. Chill Out: New Materials and Designs Keep the Chips Cool. *IEEE Spectrum*, **46**(10), pp. 28–33.
- [2] Ghosh S., Calizo I., Teweldebrhan D., Pokatilov E. P., Nika D. L., Balandin A. A., Bao W., Miao F., Lau C. N., Ghosh S., Calizo I., Teweldebrhan D., Pokatilov E. P., Nika D. L., Balandin A. A., 2008. Extremely High Thermal Conductivity of Graphene: Prospects for Thermal Management Applications in Nanoelectronic Circuits. *Applied Physics Letters*, **92**(15), p. 151911.
- [3] Balandin A. A., Ghosh S., Bao W., Calizo I., Teweldebrhan D., Miao F., Lau C. N., 2008. Superior Thermal Conductivity of Single-Layer Graphene. *Nano Letters*, **8**(3), pp. 902–907.

- [4] Chen S., Moore A. L., Cai W., Suk J. W., An J., Mishra C., Amos C., Magnuson C. W., Kang J., Shi L., Ruoff R. S., 2011. Raman Measurements of Thermal Transport in Suspended Monolayer Graphene of Variable Sizes in Vacuum and Gaseous Environments. *ACS Nano*, **5**(1), pp. 321–328.
- [5] Lee C., Wei X., Kysar J. W., Hone J., 2008. Measurement of the Elastic Properties and Intrinsic Strength of Monolayer Graphene. *Science* (New York, N.Y.) **321**(5887), pp. 385–388.
- [6] Novoselov K. S., Geim A. K., Morozov S. V., Jiang D., Zhang Y., Dubonos S. V., Grigorieva I. V., Firsov A. A., 2000. Electric Field Effect in Atomically Thin Carbon Films, doi: 10.1126/science.1102896.
- [7] Jeon C. H., Jeong Y. H., Seo J. J., Tien H. N., Hong S. T., Yum Y. J., Hur S. H., Lee K. J., 2014. Material Properties of Graphene/Aluminum Metal Matrix Composites Fabricated by Friction Stir Processing. *International Journal of Precision Engineering and Manufacturing*, **15**(6), pp. 1235-1239.
- [8] Yan S. J., Yang C., Hong Q. H., Chen J. Z., Liu D. B., Dai S. L., 2014. Research of Graphene-Reinforced Aluminum Matrix Nanocomposites. *Cailiao Gongcheng/Journal of Materials Engineering*, **0**(4), pp. 1–6.
- [9] Liu J., Khan U., Coleman J., Fernandez B., Rodriguez P., Naher S., Brabazon D., 2016. Graphene Oxide and Graphene Nanosheet Reinforced Aluminium Matrix Composites: Powder Synthesis and Prepared Composite Characteristics. *Materials & Design*, **94**, pp. 87–94.
- [10] Shin S. E., Choi H. J., Shin J. H., Bae D. H., 2015. Strengthening Behavior of Few-Layered Graphene/Aluminum Composites. *Carbon*, **82**, pp. 143-151.
- [11] Huang Y., Ouyang Q., Guo Q., Guo X., Zhang G., Zhang D., 2016. Graphite Film/Aluminum Laminate Composites with Ultrahigh Thermal Conductivity for Thermal Management Applications. *Materials & Design*, **90**, pp. 508-515.
- [12] Zheng Z., Liu Y., Bai Y., Zhang J., Han Z., Ren L., 2016. Fabrication of Biomimetic Hydrophobic Patterned Graphene Surface with Ecofriendly Anti-Corrosion Properties for Al Alloy. *Colloids and Surfaces A: Physicochemical and Engineering Aspects*, **500**, pp. 64-71.
- [13] Zhang L., Hou G., Zhai W., Ai Q., Feng J., Zhang L., Si P., Ci L., 2018. Aluminum/Graphene Composites with Enhanced Heat-Dissipation Properties by in-Situ Reduction of Graphene Oxide on Aluminum Particles. *Journal of Alloys and Compounds*, **748**, pp. 854-860.
- [14] Liu J., Hua L., Li S., Yu M., 2015. Graphene Dip Coatings: An Effective Anticorrosion Barrier on Aluminum. *Applied Surface Science*, **327**, pp. 241-245.
- [15] Han X., Huang Y., Gao Q., Yu M., Chen X., 2018. High Thermal Conductivity and Mechanical Properties of Nanotube@Cu/Ag@Graphite/Aluminum Composites. *Industrial & Engineering Chemistry Research*, **57**(31), pp. 10365-10371.
- [16] Abhinav C., Reddy K. V. K., Raju G. G., Subramanyam K., 2017. Experimental Investigation of Graphene Coated Al Cuboid Crammed with PCMs for Efficient Thermal Energy Storage and Conversion. *International Research Journal of Engineering and Technology*, **4**(12), pp. 396-402.
- [17] Su R., Zhang X., 2018. Size Effect of Thermal Conductivity in Monolayer Graphene. *Applied Thermal Engineering*, **144**, pp. 488-494.
- [18] Cao A., 2012. Molecular Dynamics Simulation Study on Heat Transport in Monolayer Graphene Sheet with Various Geometries. *Journal of Applied Physics*, **111**(8), p. 083528.
- [19] Erturk A. S., Kirca M., Kirkayak L., 2018. Mechanical Enhancement of an Aluminum Layer by Graphene Coating. *Journal of Materials Research* **33**(18), pp. 2741-2751.
- [20] Nosé S., 1984. A Unified Formulation of the Constant Temperature Molecular Dynamics Methods. *The Journal of Chemical Physics*, **81**(1), pp. 511-519.
- [21] Kumar S., 2017. Graphene Engendered 2-D Structural Morphology of Aluminium Atoms: Molecular Dynamics Simulation Study. *Materials Chemistry and Physics*, **202**, pp. 329-339.
- [22] Wei Z., Ni Z., Bi K., Chen M., Chen Y., 2011. In-Plane Lattice Thermal Conductivities of Multilayer Graphene Films. *Carbon*, **49**(8), pp. 2653-2658.
- [23] Rajasekaran G., Kumar R., Parashar A., 2016. Tersoff Potential with Improved Accuracy for Simulating Graphene in Molecular Dynamics Environment. *Materials Research Express*, **3**(3), p. 035011.
- [24] Deyirmenjian V. B., Heine V., Payne M. C., Milman V., Lynden-Bell R. M., Finnis M. W., 1995. Ab Initio Atomistic Simulation of the Strength of Defective Aluminum and Tests of Empirical Force Models. *Physical Review B*, **52**(21), pp. 15191-15207.

- [25] Shibuta Y., Elliott J. A., 2011. Interaction between Two Graphene Sheets with a Turbostratic Orientational Relationship. *Chemical Physics Letters*, **512**, pp. 146-150.
- [26] Verlet L., 1967. Computer “Exyeriments” on Classical Fluids. I. Thermodynamical Properties of Lennard-Jones Molecules. *Physical Review*, **159**(2), pp. 183-195.
- [27] Anderson C. V. D. R., Tamma K. K., 2004. An Overview of Advances in Heat Conduction Models and Approaches for Prediction of Thermal Conductivity in Thin Dielectric Films. *International Journal of Numerical Methods for Heat and Fluid Flow*, **14**(1), pp. 12-65.
- [28] Jain A., McGaughey A. J. H., 2016. Thermal Transport by Phonons and Electrons in Aluminum, Silver, and Gold from First Principles. *Physical Review B*, **93**(8), p. 081206.
- [29] Chantrenne, Raynaud, Barrat, 2003. Study of Phonon Heat Transfer in Metallic Solids from Molecular Dynamics Simulations. *Microscale Thermophysical Engineering*, **7**(2), pp. 117-136.

